

Contents

2	1 Introduction	3
3	2 Pixel detectors	5
4	2.1 Signal formation	5
5	2.2 CCDs	7
6	2.3 Hybrid pixels	7
7	2.4 CMOS MAPS and DMPAS	8
8	2.4.1 DMAPS: large and small fill factor	9
9	2.4.2 A modified sensor	11
10	2.5 Analog front end	11
11	2.5.1 Preamplifier	11
12	2.6 Readout logic	13
13	3 Use of pixel detectors	17
14	3.1 Tracking in HEP	17
15	3.1.1 Hybrid pixels at LHC and at SuperKEKB	18
16	3.1.2 First attempts to MAPS	20
17	3.2 Other applications	22
18	3.2.1 Applicability to FLASH radiotherapy	22
19	4 TJ-Monopix1	26
20	4.1 The sensor	27
21	4.2 Front end	29
22	4.2.1 ALPIDE-like	30
23	4.3 Readout logic	31
24	5 Arcadia-MD1	35
25	5.1 The sensor	35
26	5.2 Readout logic and data structure	36
27	5.2.1 Matrix division and data-packets	36
28	6 Characterization	39
29	6.1 TJ-Monopix1 characterization	39
30	6.1.1 Threshold and noise: figure of merit for pixel detectors	39
31	6.1.2 Linearity of the ToT	42
32	6.1.3 Calibration of the ToT	44
33	6.1.4 PMOS flavor: changing the bias	47
34	6.1.5 Measurements with radioactive sources	49

35	6.1.6	Dead time measurements	50
36	6.2	ARCADIA-MD1 characterization	51
37	7	Test beam measurements	53
38	7.1	Apparatus description	53
39	7.1.1	Accelerator	54
40	7.1.2	Mechanical carriers	55
41	7.2	Measurements	55
42	7.2.1	MIP spectrum using cosmic rays as source	60
43	A	Pixels detector: a brief overview	61
44	A.1	Radiation damages	61
45	Bibliography		64
46	Characterization of monolithic CMOS pixel sensors for charged particle detectors and		
47	for high intensity dosimetry		

⁴⁸

Chapter 1

⁴⁹

Introduction

⁵⁰ Since the 1980s, when the fabrication of device with very small electrodes (50-100 μm)
⁵¹ became a practical possibility, pixel detectors have been widely employed for imaging and
⁵² tracking charged particles in the vertex region of experiments at accelerators. Thanks
⁵³ to their excellent spatial resolution, today even better than 10 μm , they allow for true
⁵⁴ three-dimensional space-point determination even at high particle fluxes and in particular
⁵⁵ for the identification of secondary vertices of short-lived particles such as τ and B mesons.
⁵⁶ Requirement imposed by accelerator are stringent and they will become even more with the
⁵⁷ increase of luminosity; in this scenario CMOS Monolithic Active Pixel Sensors (MAPS) are
⁵⁸ being developed to improve the performance of the hybrid pixel detectors, which currently
⁵⁹ constitute the state-of-art for large scale pixel detector, in particular by reducing the
⁶⁰ amount of material, power consumption and pixel dimension.

⁶¹ Experiments such as ALICE at LHC and STAR at RHIC have already introduced the
⁶² CMOS MAPS technology in their detectors. ALICE Tracking System (ITS2), upgraded
⁶³ during the LHC long shut down in 2019-20, was the first large-area ($\sim 10 \text{ m}^2$) silicon vertex
⁶⁴ detector based on CMOS MAPS. Thanks to the reduction of the material budget, ITS2,
⁶⁵ which uses the ALPIDE chip developed by ALICE collaboration, obtained an amazing im-
⁶⁶ provement both in the position measurement and in the momentum resolution, improving
⁶⁷ the efficiency of track reconstruction for particle with very low transverse momentum (by
⁶⁸ a factor 6 at $p_T \sim 0.1 \text{ GeV}/c$). Further advancements in CMOS MAPS technology are
⁶⁹ being aggressively pursued for the ALICE ITS3 and the Belle II vertex detector upgrades
⁷⁰ (both foreseen around 2026-27) and by the R&D53 collaboration for the upgrade at HL-
⁷¹ LHC, with the goals of further reducing the sensor thickness and improving the readout
⁷² speed of the devices, while keeping power consumption at a minimum.

⁷³ Beside tracking, the development of pixel detectors is a very active field with many
⁷⁴ applications: a noteworthy example of detector originally used in particle physics, and
⁷⁵ later employed mainly for medical imaging, but also in space and for art authentication, is
⁷⁶ Medipix, a hybrid system developed at CERN within the Medipix collaboration. Among
⁷⁷ medical applications, a possible use of CMOS MAPS could be in dosimetry: in the last few
⁷⁸ years the search of radiotherapy oncological treatments with high intensity beams (FLASH
⁷⁹ mode) is requiring new dosimeters, both for the therapies as well as new beam-monitors
⁸⁰ (especially for focused very high energy electron beams), which are capable of deal with
⁸¹ extreme dose rate (up to 40 Gy/s).

⁸² I've studied the characteristics of two ALPIDE-like CMOS MAPS chips and tested
⁸³ them under different front end configuration. The first chip, the TJ-Monopix1 from the

84 Monopix series, is a TowerJazz MAPS fabricated in 180 nm CMOS technology and is one
85 of the prototypes for the Belle II vertex detector upgrade. The second chip, called Main
86 Demonstrator-1, is produced by LFoundry in 110 nm CMOS technology and designed by
87 the ARCADIA (Advanced Readout CMOS Architectures with Depleted Integrated sensor
88 Arrays) group; it is intended to be a general purpose device with possible use in medical
89 scanners, space experiments, future lepton colliders and also possibly X-ray applications
90 with thick substrates. The main differences between the two chips are in the output signal
91 type and in the readout sequence of the matrix. Concerning the former point while TJ-
92 Monopix1 returns an analog output information, that is the time over threshold of the
93 pulse which can be related with the charge released by the particle in the , MD1 returns
94 only a digital information if a hit has been; regarding the latter, instead, TJ-Monopix1
95 has a completely sequential readout, while MD1 grossly combines the information of the
96 hits in order to reduce the data transmission time and reduce the dead time.

97 I have set up two test systems for the two chips in the INFN clean laboratories and
98 characterized the devices electrically and with radioactive sources. In particular I have
99 performed the characterization of the chips to find the threshold and noise of the pixels
100 and their dispersion across the matrix, to have an absolute value in electrons of the signal
101 recorded by TJ-Monopix1, I've also performed an absolute calibration using a Fe55 x-ray
102 source and studied the dead time and the readout properties. Moreover, I've also test
103 TJ-Monopix1 at high dose rate with the FLASH-accelerator recently installed at Santa
104 Chiara hospital in Pisa, and I have participated in the design of the setup needed for test
105 beam measurement.

¹⁰⁶ **Chapter 2**

¹⁰⁷ **Pixel detectors**

¹⁰⁸ Pixel detectors are members of the semiconductor detectors and their operation is based on
¹⁰⁹ the creation of electron-hole couples in the bulk by the particle impinging which are then
¹¹⁰ separated and drifted by the electric field and collected at their respectively electrodes.
¹¹¹ The applied electric field, the depletion zone thickness, the front end, the processing and
¹¹² the transmittion of the signal are specific charateristics of each particular chip. In this
¹¹³ chapter I am going to discuss the main kinds of pixel detectors, dwelling specifically on
¹¹⁴ Monolithic Active Pixels (MAPS).

¹¹⁵ **2.1 Signal formation**

¹¹⁶ When a charge particle passes through a pixel and loses energy by ionization only a part
¹¹⁷ of that energy is used to generate electron-hole pairs, since another part is used for other
¹¹⁸ processes, as the lattice excitation. The average energy needed to create a pair at 300K
¹¹⁹ in silicon is $w_i = 3.65 \text{ eV}$, that is more than the mean ionization energy because of the
¹²⁰ interactions with phonon, since for a minimum ionizing particle (MIP) the most probable
¹²¹ value (MPV) of charge released in the semiconductor is $0.28 \text{ keV}/\mu\text{m}$, hence the number
¹²² of electrons-vacuum pairs is:

$$\langle \frac{dE}{dx} \rangle \frac{1}{w_i} \sim 80 \text{ e}/h \sim \frac{1.28 \cdot 10^{-2} fC}{\mu\text{m}} \quad (2.1)$$

¹²³ Because of the splitting of the energy depositon between the two different processes, the
¹²⁴ number of the couples generated undergoes fluctuations that usually follow a Poisson
¹²⁵ distribution. Thus the fluctuations of the number of generated e/h pairs is equal to
¹²⁶ $\sigma_{e/h} = \sqrt{N_{e/h}}$. Under the constraint of complete absorption of a particle the energy
¹²⁷ resolution improves of a factor \sqrt{F} , where F is called the Fano factor and determines the
¹²⁸ ultimate limit of energy resolution for semiconductors and is a function of the material
¹²⁹ and temperature and for silicon is equal to $F_{\text{Si}} \sim 0.115$.

¹³⁰ It is fundamental that pairs e/h are produced in the depleted region of the semicon-
¹³¹ ductor where the probability of recombination with charge carriers is low to avoid loss of
¹³² signals. It is formed by bringing in contact an n-doped and a p-doped silicon crystal. For
¹³³ this reason pixel detectors are then commonly reverse biased: a positive bias is given to
¹³⁴ the n electrode and a negative to the p in order to grow the depletion zone in the epitaxial
¹³⁵ layer within the bulk.

¹³⁶ At the boundary between the two types, the majority carriers diffuse to the opposite
¹³⁷ part where they recombine. Therefore, a space charge region depleted of free carriers

138 is formed. The positively charged donor ions and negatively charged acceptor ions that
 139 remain in the n-type and p-type regions respectively cause an electric field to build up
 140 across the junction. The majority charge carrier diffusion is opposed by the generated
 electric field and the junction reaches an equilibrium state.

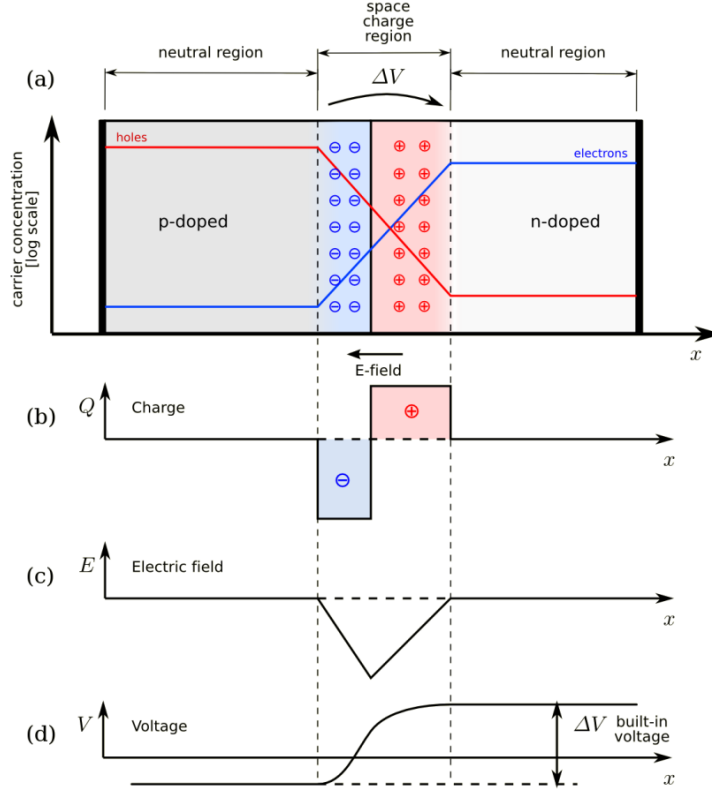


Figure 2.1: The structure of an (abrupt) p-n junction: (a) structure, (b) space charge density, (c) electric field distribution and (d) potential distribution.

141
 142 The width of the depletion region is related with the external bias V_{ext} , the resistivity
 143 ρ and also with the dopant:

$$d_n \sim 0.55 \sqrt{\frac{\rho}{\Omega cm} \frac{V_{ext}}{V}} \mu m \quad (2.2) \quad d_p \sim 0.32 \sqrt{\frac{\rho}{\Omega cm} \frac{V_{ext}}{V}} \mu m \quad (2.3)$$

144

146

147 For that reason high resistivity wafers ($100 \Omega cm - k\Omega cm$) are typically preferred be-
 148 cause they allow bigger depletion zone with smaller voltage bias.

149 The charges created are then separated by the electric field and collected at their re-
 150 spectively electrodes (p for holes and n for electrons)¹; by the drift of these charges, a
 151 signal i_e is generated on the electrode e as stated by the Shockley-Ramo's theorem:

$$i_e(t) = -q v(t) E_{WF,e} \quad (2.4)$$

¹Even if in principle both the electrode can be used to read the signal, for pixel detectors, where the number of channel and the complexity of readout are high, only one is actually used. In strip and pad detectors, instead, is more common a dual-side readout

152 where $v(t)$ is the instantaneous velocity of the charge q and E_{WF} is the weighting field,
 153 that is the field obtained biasing the electrode e with 1V and all the others with 0V. The
 154 drift velocity of the charge depends on the electric field and on the mobility of the particle:

$$v = \mu(E) E \quad (2.5)$$

155 where $\mu(E)$ is a function of the electric field and is linear with E only for small E : at
 156 higher values the probability of interactions with optical phonons increases, the mobility
 157 drops and this leads to an independence of the velocity from the electric field (fig. 2.2).

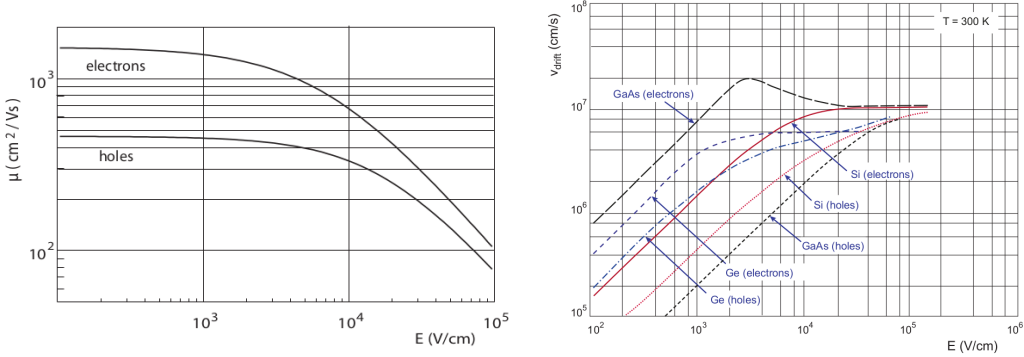


Figure 2.2: (a) Typical values for electrons and holes mobility in silicon at room temperature are $\mu_n \sim 1450 \text{ cm}^2/\text{Vs}$, $\mu_h = 500$. (b) Drift velocity at room temperature in different semiconductors

158 2.2 CCDs

159 **descrivi come sono fatte e come funziona il readout** Tens of ms due to the need to transfer
 160 the charge signals pixel by pixel through a single output circuit For photon imaging the
 161 need of high assorbtion efficiency, **per cui usi materiali con alto Z**

162 2.3 Hybrid pixels

163 **METTI IN EVIDENZAZ CHE PUOI FARE UN READOUT CON TECNOLOGIA CMOS.**
 164 **Metti in evidenza che sono più veloci** Hybrid pixels are made of two parts (fig. 2.3a), the
 165 sensor and the electronics: for each pixel these two parts are welded together through
 166 microconnection (bump bond).
 167 They provide a practical system where readout and sensor can be optimized separately,
 168 although the testing is less easy-to-do since the sensor and the R/O must be connected
 169 together before.
 170 In addition, the particular and sophisticated procedure to bond sensor and ASIC (applica-
 171 tion specific integrated circuit) makes them difficult to produce, delicate, especially when
 172 exposed to high levels of radiation, and also expensive.
 173 A critical parameter for accelerator experiments is the material budget, which represents
 174 the main limit factor for momentum measurement resolution in a magnetic field; since
 175 hybrid pixels are thicker (\sim hundreds of μm) than monolithic ones (even less than 100
 176 μm), using the latter the material budget can be down by a third: typical value for hybrid
 177 pixels is 1.5 % X_0 per layer, while for monolithic 0.5 % X_0 .

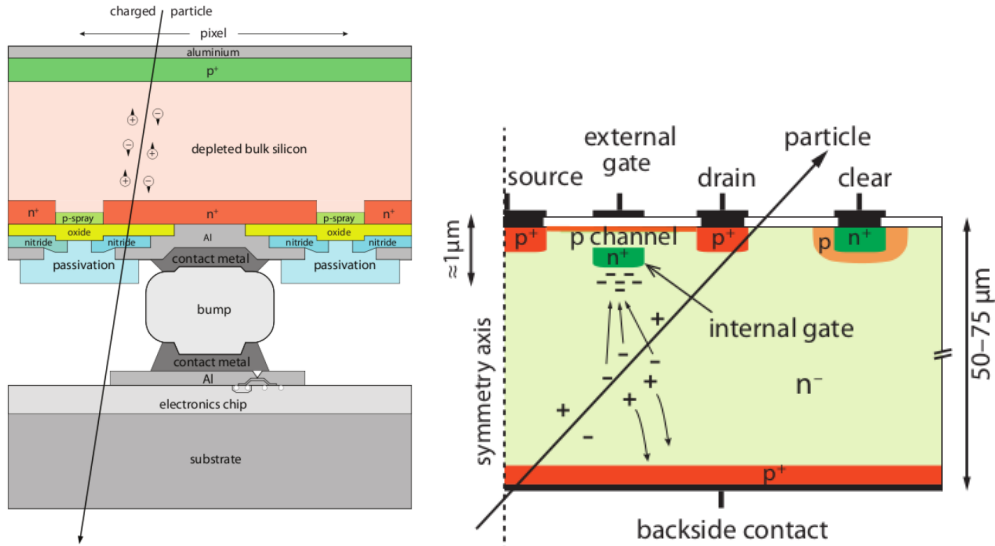


Figure 2.3: Concept cross-section of hybrid pixel (a) and of a DEPFET (b)

178 Among other disadvantages of hybrid pixels there is the bigger power consumption that
 179 implies, by the way, a bigger cooling system leading in turn to an increase in material too.
 180

181 DEPFET are the first attempt towards the integration of the front end (FE) on the
 182 sensor bulk: they are typically mounted on a hybrid structure but they also integrate the
 183 first amplification stage.

184 Each pixel implements a MOSFET (metal-oxide-semiconductor field-effect transistor) trans-
 185 sistor (a p-channel in fig. 2.3b): an hole current flows from source to drain which is con-
 186 trolled by the external gate and the internal gate together. The internal gate is made by a
 187 deep n+ implant towards which electrons drift after being created in the depletion region
 188 (to know how the signal is created in a pixel detector look at appendix A); the accumu-
 189 lation of electrons in the region underneath the n implant changes the gate potential and
 190 controls the transistor current.

191 DEPFET typically have a good S/N ratio: this is principally due the amplification on-
 192 pixel and the large depletion region. But, since they need to be connected with ASIC the
 193 limiting factor still is the material budget.

194 2.4 CMOS MAPS and DMPAS

195 With respect to CCDs, the radiation tolerance could be greatly increased by sensing the
 196 signal charge within its own pixel, instead of transporting it over thousands of pixels. The
 197 readout speed could also be dramatically increased by in-pixel amplitude discrimination,
 198 followed by sparse readout of only the hit pixels. Monolithic active pixels accommodate
 199 on the same wafer both the sensor and the front end electronics, with the second one
 200 implanted on top within a depth of about 1 μm below the surface.

201 MAPS have been first proposed and realized in the 1990s and their usage has been en-
 202 abled by the development of the electronic sector which guarantees the decrease in CMOS
 203 transistors dimension at least every two years, as stated by the Moore's law².

²Moore's law states that logic density doubles every two years.

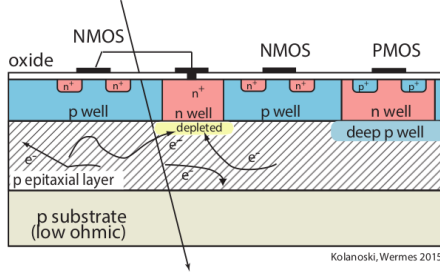


Figure 2.4: Concept cross-section of CMOS MPAS pixel

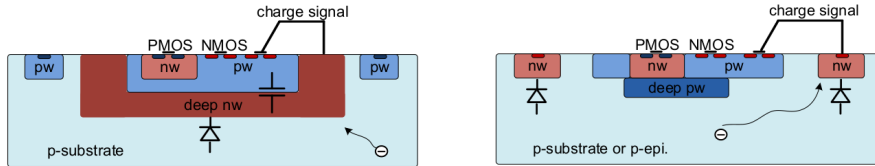


Figure 2.5: Concept cross-section with large and small fill factor

204 As a matter of fact the dimension of components, their organization on the pixel area
 205 and logic density are important issues for the design and for the layout; typically different
 206 decisions are taken for different purposes.

207 Monolithic active pixel can be distinguished between two main categories: MAPS and
 208 depleted MAPS (DMAPS).

209 MAPS (figure a.2.4) have typically an epitaxial layer in range $1\text{ }\mu\text{m}$ to $20\text{ }\mu\text{m}$ and because
 210 they are not depleted, the charge is mainly collected by diffusion rather than by drift.
 211 This makes the path of charges created in the bulk longer than usual, therefore they are
 212 slow (of order of 100 ns) and the collection could be partial especially after the irradiation
 213 of the detector (look at A for radiation damages), when the trapping probability become
 214 higher.

215 In figure 2.4 is shown as example of CMOS MAPS: the sensor in the scheme implements
 216 an n well as collection diode; to avoid the others n wells (which contain PMOS transistor)
 217 of the electronic circuit would compete in charge collection and to shield the CMOS circuit
 218 from the substrate, additionally underlying deep p well are needed. DMAPS are instead
 219 MAPS depleted with d typically in $\sim 25\text{ }\mu\text{m}$ to $150\text{ }\mu\text{m}$ (eq. 2.1) which extends from the
 220 diode to the deep p-well, and sometimes also to the backside (in this case if one wants to
 221 collect the signal also on this electrode, additional process must be done).

222 2.4.1 DMAPS: large and small fill factor

223 There are two different sensor-design approaches (figure 2.5) to DMAPS:

- 224 • large fill factor: a large collection electrode that is a large deep n-well and that host
 225 the embedded electronics
- 226 • small fill factor: a small n-well is used as charge collection node

227 To implement a uniform and stronger electric field, DMAPS often uses large electrode
 228 design that requires multiple wells (typically four including deep n and p wells); this layout
 229 adds on to the standard terms of the total capacity of the sensor a new term (fig. 2.6),

	small fill factor	large fill factor
small sensor C	✓ (< 5 fF)	✗ (~ 100 200fF)
low noise	✓	✗
low cross talk	✓	✗
velocity performances	✓	✗ (~100 ns)
short drift paths	✗	✓
radiation hard	✗	✓

Table 2.1: Small and large fill factor DMAPS characteristics

that contributes to the total amplifier input capacity. In addition to the capacity between pixels (C_{pp}) and between the pixel and the backside (C_b), a non-negligible contribution comes from the capacities between wells (C_{SW} and C_{WW}) needed to shield the embedded electronics. These capacities affect the thermal and 1/f noise of the charge amplifier and the τ_{CSA} too:

$$ENC_{thermal}^2 \propto \frac{4}{3} \frac{kT}{g_m} \frac{C_D^2}{\tau_{sh}} \quad (2.6) \quad \tau_{CSA} \propto \frac{1}{g_m} \frac{C_D}{C_f} \quad (2.7)$$

where g_m is the transconductance, τ_{sh} is the shaping time.

Among the disadvantages coming from this large input capacity could be the coupling between the sensor and the electronics resulting in cross talk: noise induced by a signal on neighbouring electrodes; indeed, since digital switching in the FE electronics do a lot of oscillations, this problem is especially connected with the intra wells capacities. So, larger

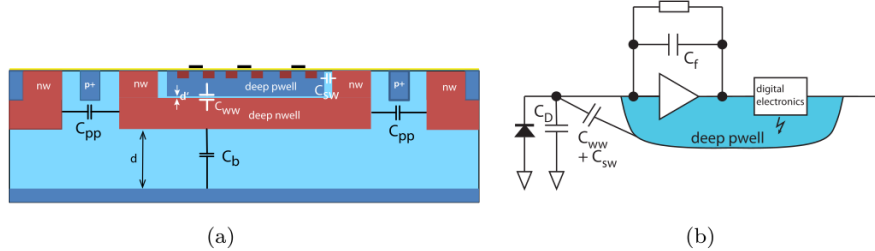


Figure 2.6: C_{pp} , C_b , C_{WW} , C_{SW}

charge collection electrode sensors provide a uniform electric field in the bulk that results in short drift path and so in good collection properties, especially after irradiation, when trapping probability can become an issue. The drawback of a large fill-factor is the large capacity (~100 fF): this contributes to the noise and to a speed penalty and to a larger possibility of cross talk.

The small fill-factor variant, instead, benefits from a small capacity (5 fF to 20 fF), but suffers from a not uniform electric field and from all the issue related to that. **Ho già detto prima parlando dei MAPS, devo ripetere qui?**

As we'll see these two different types of sensor require different amplifier: the large electrode one is coupled with the charge sensitive amplifier, while the small one with voltage amplifier (sec 2.5.1).

252 **2.4.2 A modified sensor**

253 A process modification developed by CERN in collaboration with the foundries has become
254 the standard solution to combine the characteristics of a small fill factor sensor (small input
255 amplifier capacity) and of large fill factor sensor (uniform electric field) is the one carried
256 out for ALICE upgrade about ten years [1].

257 A compromise between the two sensors could also be making smaller pixels, but this
258 solution requires reducing the electronic circuit area, so a completely new pixel layout
259 should be though. The modification consists in inserting a low dose implant under the
260 electrode and one its advantage lies in its versatility: both standard and modified sensor
261 are often produced for testing in fact.

262 Before the process modification the depletion region extends below the diode towards
263 the substrate, and it doesn't extend laterally so much even if a high bias is applied to the
264 sensor (fig. 2.7).

265 After, two distinct pn junctions are built: one between the deep p well and the n^- layer,
266 and the other between the n^- and the p^- epitaxial layer, extending to the all area of the
267 sensor.

268 Since deep p well and the p-substrate are separated by the depletion region, the two p
269 electrodes can be biased separately³ and this is beneficial to enhance the vertical electric
270 field component.

271 The doping concentration is a trimmer parameter: it must be high enough to be greater
272 than the epitaxial layer to prevent the punchthrough between p-well and the substrate,
273 but it must also be lower enough to allow the depletion without reaching too high bias.

274 **2.5 Analog front end**

275 After the creation of a signal on the electrode, the signal enters the front end circuit
276 (fig.2.8), ready to be molded and transmitted out of chip. Low noise amplification, fast
277 hit discrimination and an efficient, high-speed readout architecture, consuming as low
278 power as possible must be provided by the readout integrated electronics (ROIC).

279 Let's take a look to the main steps of the analog front end chain: the preamplifier (that
280 actually often is the only amplification stage) with a reset to the baseline mechanism and
281 a leakage current compensation, a shaper (a band-pass filter) and finally a discriminator.
282 The whole chain must be optimized and tuned to improve the S/N ratio: it is very impor-
283 tant both not to have a large noise before the amplification stage in order to not multiply
284 that noise, and chose a reasonable threshold of the discriminator to cut noise-hits much
285 as possible.

286 **2.5.1 Preamplifier**

287 Even if circuits on the silicon crystal are only constructed by CMOS, a preamplifier can be
288 modeled as an operational amplifier (OpAmp) where the gain is determined by the input
289 and feedback impedance (first step in figure 2.8):

$$G = \frac{v_{out}}{v_{in}} = \frac{Z_f}{Z_{in}} \quad (2.8)$$

³This is true in general, but it can be denied if other doping characteristics are implemented, and we'll see that this is the case of TJ-Monopix1

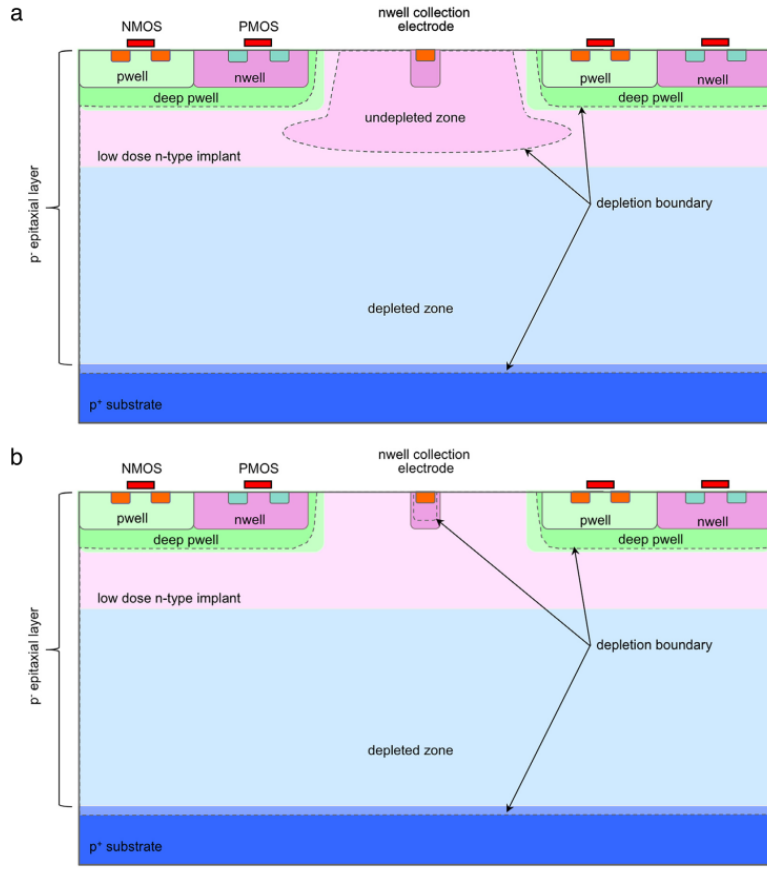


Figure 2.7: A modified process for ALICE tracker detector: a low dose n implant is used to create a planar junction. In (a) the depletion is partial, while in (b) the pixel is fully depleted.

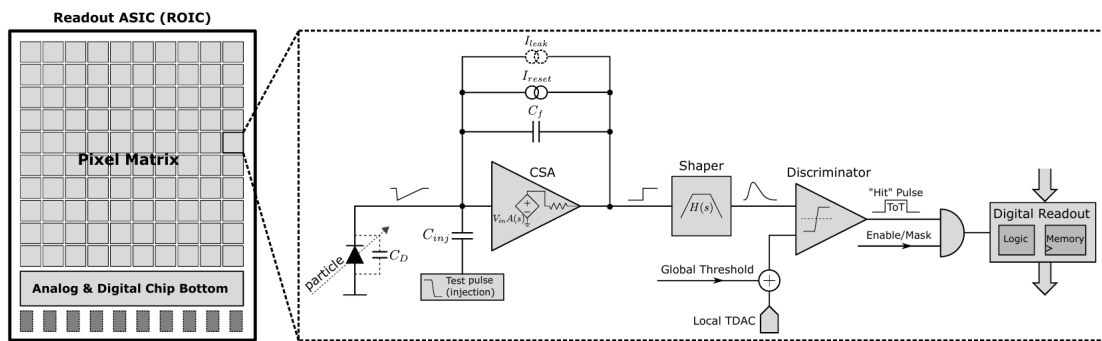


Figure 2.8: Readout FE scheme: in this example the preamplifier is a charge sensitive one (CSA) but changing the capacitive feedback into a resistive one, this can be converted in a voltage or current amplifier.

290 Depending on whether a capacity or a resistance is used as feedback, respectively a charge
 291 or a voltage amplifier is used: if the voltage input signal is large enough and have a sharp
 292 rise time, the voltage sensitive preamplifier is preferred. Consequently, this flavor doesn't
 293 suit to large fill factor MAPS whose signal is already enough high: $v_{in} = Q/C_D \approx 3fC/100$
 294 pF = 0.03 mV, but it's fine for the small fill factor ones: $v_{in} = Q/C_D \approx 3fC/3$ pF = 1
 295 mV.

296 In the case of a resistor feedback, if the signal duration time is longer than the discharge
 297 time ($\tau = R_S C_D$) of the detector the system works as current amplifier, as the signal is
 298 immediately transmit to the amplifier; in the complementary case (signal duration longer
 299 than the discharge time) the system integrates the current on the C_D and operates as a
 300 voltage amplifier.

301 2.6 Readout logic

302 Readout logic includes the part of the circuit which takes the FE output signal, processes
 303 it and then transmit it out of pixel and/or out of chip; depending on the situation of usage
 304 different readout characteristics must be provided.

305 To store the analogical information (i.e. charge collected, evolution of signal in time, ...) big
 306 buffers and a large bandwidth are needed; the problem that doesn't occur, or better
 307 occur only with really high rate, if one wants record only digital data (if one pixel is hit
 308 1 is recorded, and if not 0 is recorded).

309 A common compromise often made is to save the time over threshold (ToT) of the pulse
 310 in clock cycle counts; this needs of relatively coarse requirement as ToT could be trimmer
 311 to be a dozen bits but, being correlated and hopefully being linear with the deposited
 312 charge by the impinging particle in the detector, it provides a sufficient information. The
 313 ToT digitalization usually takes advantage of the distribution of a clock (namely BCID,
 314 bunch crossing identification) on the pixels' matrix. The required timing precision is at
 315 least around 25 ns, that corresponds to the period of bunch collisions at LHC; for such
 316 reason a reasonable BCID-clock frequency for pixels detector is 40 MHz.

317 Leading and trailing edges' timestamp of the pulse are saved on pixel within a RAM until
 they have been read, and then the ToT is obtained from their difference.

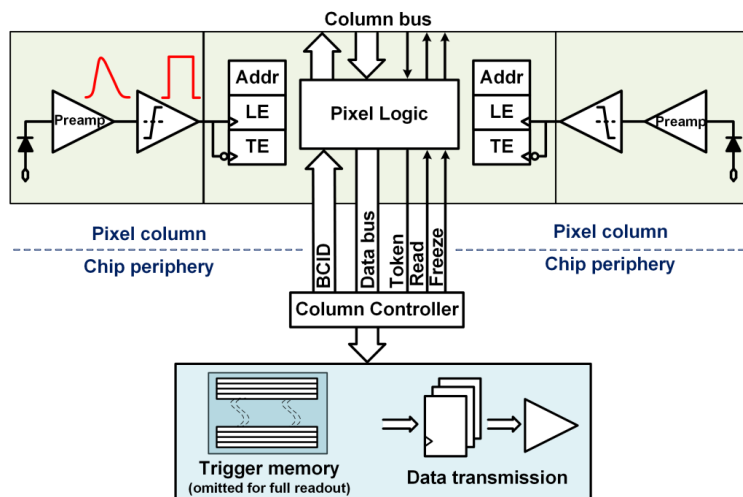


Figure 2.9: Column drain R/O scheme where ToT is saved

319 Moreover, the readout architecture can be full, if every hit is read, or triggered, if a
 320 trigger system decides if the hit must be store or not. On one hand the triggered-readout
 321 needs buffers and storage memories, on the other the full readout, because there is no need
 322 to store hit data on chip, needs an high enough bandwidth.

323 A triggered readout is fundamental in accelerator experiments where the quantity of data
 324 to store is too large to be handled, and some selections have to be applied by the trigger:
 325 to give an order of growth, at LHC more than 100 TBit/s of data are produced, but the
 326 storage limit is about 100 MBit/s [2] (pag. 797).

327 Typically the trigger signal is processed in a few μs , so the pixel gets it only after a
 328 hundred clock cycles from the hit arrival time: the buffer depth must than handle the
 329 higher trigger latency.

330 After having taken out the data from the pixel, it has to be transmitted to the end of
 331 column (EoC) where a serializer deliver it out of chip, typically to an FPGA.

332 There are several ways of transmitting data from pixel to the end of column: one of the
 333 most famous is the column-drain read out, developed for CMS and ATLAS experiments
 334 [3]. All the pixels in a double-column share a data bus and only one pixel at a time,
 335 according to a priority chain, can be read. The reading order circuit is implemented by
 336 shift register (SR): when a hit arrives, the corresponding data, which can be made of
 337 timestamp and ToT, is temporarily stored on a RAM until the SH does not allow the
 338 access to memory by data bus.

339 Even if many readout architectures are based the column-drain one, it doesn't suit for
 340 large size matrices. The problem is that increasing the pixels on a column would also
 341 raise the number of pixels in the priority chain and that would result in a slowdown of the
 342 readout.

343 If there isn't any storage memory, the double-column behaves as a single server queue
 344 and the probability for a pixel of waiting a time T greater than t , with an input hit rate
 345 on the column μ and an output bandwidth B_W is [4]:

$$P(T > t) = \frac{\mu}{B_W} e^{-(B_W - \mu)t} \quad (2.9)$$

346 To avoid hit loss (let's neglect the contribution to the inefficiency of the dead time τ due
 347 to the AFE), for example imposing $P_T > t \sim 0.001$, one obtains $(B_W - \mu) t_t \sim 6$, where
 348 t_t is the time needed to transfer the hit; since t_t is small, one must have $B_W \gg \mu$, that
 means a high bandwidth [4].

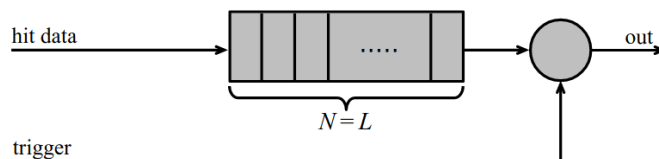


Figure 2.10: Block diagram of a pipeline buffer: N is the dimension of memory buffer and L is the trigger latency expressed in BCID cycles

349
 350 Actually the previous one is an approximation since each pixel sees a different band-
 351 width depending on the position on the queue: the first one sees a full bandwidth, but
 352 the next sees a smaller one because occasionally it can be blocked by the previous pixel.
 353 Then the bandwidth seen by the pixel i is $B_i = B - \sum_j \mu_j$, where μ_j is the hit rate of the
 354 j th pixel.

355 The efficiency requirement on the bandwidth and the hit rate becomes: $B_{W,i} > \mu_i$, where
 356 the index i means the constraint is for a single pixel; if all the N pixels on a column have
 357 the same rate $\mu = N\mu_i$, the condition reduces to $B_W > \mu$. The bandwidth must be chosen
 358 such that the mean time between hits of the last pixel in the readout chain is bigger than
 359 that.

360 In order to reduce the bandwidth a readout with zero suppression on pixel is typically
 361 employed; this means that only information from channels where the signal exceeds the
 362 discriminator threshold are stored. Qu'è la zero suppression? La metto qui questa
 363 affermazione?

364 If instead there is a local storage until a trigger signal arrives, the input rate to column
 365 bus μ' is reduced compared to the hit rate μ as: $\mu' = \mu \times r \times t$, where r is the trigger rate
 366 and t is the bunch crossing period. In this situation there is a more relaxed constraint
 367 on the bandwidth, but the limiting factor is the buffer depth: the amount of memory
 368 designed depends both on the expected rate μ and on the trigger latency t as $\propto \mu \times t$,
 369 that means that the higher the trigger latency and the lower the hit rate to cope with.

370 In order to have an efficient usage of memory on pixels' area it's convenient grouping
 371 pixels into regions with shared storage. Let's compare two different situations: in the first
 372 one a buffer is located on each pixel area, while in the second one a core of four pixels
 373 share a common buffer (this architecture is commonly called FE-I4).

Consider a 50 kHz single pixel hits rate and a trigger latency of 5 μs , the probability of

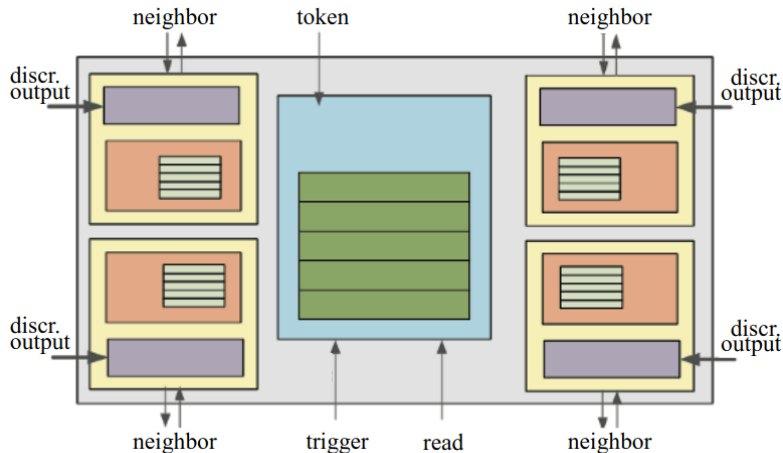


Figure 2.11: Block diagram of the FE-I4 R/O. Read and memory management section is highlighted in light blue; latency counters and trigger management section are highlighted in green; hit processing blocks are highlighted in purple; ToT counters and ToT management units are highlighted in orange

374
 375 losing hits is:

$$P(N > 1|\nu) = 1 - P(N = 0|\nu) - P(N = 1|\nu) = 1 - e^{-\nu}(1 + \nu) \approx 2.6\% \quad (2.10)$$

376 where I have assumed a Poissonian distribution with mean $\nu = 0.25$ to describe the counts
 377 N .

378 To get an efficiency ϵ greater than 99.9 % a 3 hit depth buffer is needed:

$$P(N > 3|\nu) = 1 - \sum_{i=0}^3 P(N = i|\nu) < 0.1\% \quad (2.11)$$

³⁷⁹ Considering the second situation: if the average single pixel rate is still 50 kHz, grouping
³⁸⁰ four pixels the mean number of hits per trigger latency is $\nu = 0.25 \times 4 = 1$. To get an
³⁸¹ efficiency of 99.9% (eq. 2.11) a buffer depth of 5 hits in the four-pixels region, instead of
³⁸² 3 per pixels, is needed.

³⁸³ **Chapter 3**

³⁸⁴ **Use of pixel detectors**

³⁸⁵ There always was a tight relation between the development of cameras and pixel detectors
³⁸⁶ since 1969, when the idea of CCDs, thanks to whom Boyle and Smith were awarded the
³⁸⁷ Nobel Prize in Physics in 2009, revolutionized photography allowing light to be captured
³⁸⁸ electronically instead of on film. Even though the CMOS technology was already known
³⁸⁹ when CCDs spread, the costs of productions were too high to allow the diffusion of these
³⁹⁰ sensors for which needed to wait until 1990s. From that period on, the fast diffusion of
³⁹¹ CMOS was mainly due to the less cost than CCD, and the less power required for sup-
³⁹² ply. Nowadays CCDs are still preferred over MAPS in astronomy, where the astronomical
³⁹³ sources' rate are low enough to cope with tens of ms for the readout.

³⁹⁴ The principal use cases of pixel detectors are particle tracking and imaging: in the
³⁹⁵ former case individual charged particles have to be identified, in the latter instead an
³⁹⁶ image is obtained by the usually un-triggered accumulation of the impinging radiation.
³⁹⁷ Also the demands on detectors performance depends on their usage, in particular tracking
³⁹⁸ requires high spatial resolution, fast readout and radiation hardness.

³⁹⁹ **3.1 Tracking in HEP**

⁴⁰⁰ At first the physics world overlooked the CCDs, and all pixel in general, as against the
⁴⁰¹ gaseous detector for tracking: there was no need to replace these ones which had a sufficient
⁴⁰² good resolution ($100\text{ }\mu\text{m}$). Since 1974, with the measurement of the invariant mass of the **j**
⁴⁰³ **psi** and the affirmation of the quark model, all experiments start to look for better spatial
⁴⁰⁴ resolutions in order to achieve the possibility of reconstructing short lived particle.

⁴⁰⁵ Historically, the first pixel detector employed in particle physics was a CCD: it was
⁴⁰⁶ installed in the spectrometer at the CERN's Super Proton Synchrotron (SPS) by the AC-
⁴⁰⁷ CMOR Collaboration (Amsterdam, CERN, Cracow, Munich, Oxford, RAL) at mid 1980s,
⁴⁰⁸ with the purpose of studying the recently-discovered charm particles. The second famous
⁴⁰⁹ usage of CCDs took place at SLAC in the Large Detector (SLD) during the two years
⁴¹⁰ 1996-98. **Cosa vedono di così importante da dire che servono i pixel detector?** From that
⁴¹¹ period on particle tracking in experiments have been transformed radically: it was manda-
⁴¹² tory for HEP experiments to build an inner vertex detector. In 1991, the more demanding
⁴¹³ environments led to the development of hybrid pixel detectors: a dedicated collabora-
⁴¹⁴ tion, RD19, was established at CERN with the specific goal to define a semiconductor
⁴¹⁵ micropattern detector with an incorporated signal processing at a microscopic level. In
⁴¹⁶ those years a wide set of prototypes of hybrid pixel has been manufactured; among the

417 greatest productions a mention goes to the huge ATLAS and CMS vertex detectors. From
418 the middle of 2013 a second collaboration, RD 53, has been established with the new goal
419 to find a pixel detector suitable for phase II future upgrades of those experiments. Even if
420 the collaboration is specifically focused on design of hybrid pixel readout chips (aiming to
421 65 nm tecnique so that the electronics fits within the pixel area), also other options have
422 been taken in account and many test have been done on MAPS for example. Requirements
423 imposed by HL-LHC will become tigher in time: for example, a dose and radiation
424 of 5 Mrad and 1016NIEL are exepcted after 5 years of operation. Time resolution, material
425 budget and power consumption are also issues for the upgrade: a time resolution better
426 than 25 ns for a bunch crossing frequency of 40 MHz, a material budget lower than 2%
427 and a power consunption lower than 500 mW/cm² are required.

428 Amidst the solutions proposed 3D silicon detector, invented by Sherwood Parker in
429 1995, and MAPS are the most promising. In 3D sensors the electrode is a narrow column
430 of n-type implanted vertically across the bulk instead of being implanted on the wafer's
431 surface. The charge produced by the impinging particle is then drifted transversally within
432 the pixel, and, as the mean path between two electrode can be souffcient low, the trap
433 probability is not an issue. 3D pixels have been already proved in ATLAS tracker [quando?](#).
434 Even if 3D detector are adequately radiation hard, MAPS architecture looked very promis-
435 ing from the beginning: they overcome both the CCDs long reading time and the hybrid
436 problems (I have already explained in section ?? the benefits of MAPS). Experiments
437 such as ALICE at LHC and STAR at RHIC have already introduced the CMOS MAPS
438 technology in their detectors. ALICE Tracking System (ITS2), upgraded during the LHC
439 long shut down in 2019-20, was the first large-area ($\sim 10 \text{ m}^2$ covered by 2.5 Gpixels) silicon
440 vertex detector based on CMOS MAPS.

441 3.1.1 Hybrid pixels at LHC and at SuperKEKB

442 ATLAS

443 With CMS, ATLAS is one of two general-purpose detectors at the LHC and has the largest
444 volume detector ever constructed for a particle collider (46 m long and 25 m in diameter).
445 The Inner Detector consists of three different systems all immersed in a magnetic field
446 parallel to the beam axis whose main components are: the pixel, the micro-strips and
447 transition radiation trackers. Concerning the pixel detector, 92 million pixels are divided
448 in 4 barrel layers and 3 disks in each end-cap region, covering a total area of 1.9 m² and
449 having a 15 kW of power consumption.

450 As stated by the ATLAS collaboration the pixel detector is exposed by an extreme
451 particle flux: "By the end of Run 3¹, the number of particles that will have hit the
452 innermost pixel layers will be comparable to the number it would receive if it were placed
453 only a few kilometres from the Sun during a solar flare". Considering that the particle
454 density will increase even more with HL-LHC, radiation hardness is definitively target to
455 achieve.

456 The most ambitious goal is employ a MAPS-based detector for the inner-layer barrels,
457 and for this reason the RD53 collaboration is performing many test on MAPS prototypes,
458 as Monopix of which I will talk about in section ??.

459 Up to now this possibility will be eventualy implemented during the second phase of the
460 HL-LHC era, as at the start of high-luminosity operation the selected option is the hybrid

¹Run 3 start in June 2022

461 one. The sensor will be bonded with ITkPix, the first full-scale 65 nm hybrid pixel-readout
462 chip developed by the RD53 collaboration. Regarding the sensor, a valueable option is
463 using 3D pixels, which have already proved themselves in ATLAS, for the insertable B
464 layer (IBL).**qualcosa in più sui 3d.** The number of pixels will be increased of a factor about
465 7, passing from 92 milions to 6 billion.

466 CMS

467 **da scrivere** 124 million pixels; cylindrical layers roughly at 3cm, 7cm, 11cm and 16cm
468 and disks at either end, and so will be vital in reconstructing the tracks of very short-
469 lived particles. Each of these silicon pixels is 100um by 150um,even with only around 50
470 microwatts per pixel, the total power output is 7.5kW-

471 LHCb

472 LHCb is a dedicated heavy-flavour physics experiment that exploits pp interactions at
473 14 TeV at LHC. It was the last experiment to upgrade the vertex detector, the Vertex
474 Locator (VELO), replacing the silicon-strip with pixels in May 2022. As the instantaneous
475 luminosity in Run3 is increased by a factor $\lesssim 10$, much of the readout electronics and
476 of the trigger system have been developed in order to cope with the large interaction
477 rate. To place the detector as close as possible to the beampipe and reach a better track
478 reconstruction resolution, the VELO has a surprising feature: it can be moved. During the
479 injection of LHC protons it is parket at 3 cm from the beams and only when the stability
480 is reach it is brought at ~ 5 mm. Radiation hardness as well as readout speed are then a
481 priority for the detectors: that's why the collaboration opted for a hybrid system. The
482 Velopix is made bonding sensors, each measuring 55×55 micrometers, $200 \mu\text{m}$ -thick to
483 a $200 \mu\text{m}$ -thick ASIC specially developed for LHCb and coming from the Medipix family
484 (sec. ??), which can handles hit rates up to 900 MHz per chip. Since the detector is
485 operated under vacuum near the beam pipe, the heat removal is particularly difficult and
486 evaporative CO₂ microchannel cooling are used.

487 BelleII

488 The current vertex detector of BelleII, VXD, is made of a pixel detector (PXD), fabricated
489 with 2 layers of DEPFET-based pixels, and 4 layers of a double-sided silicon strip detectors
490 (SVD)[5]. Due to the small capacitance of the collection node, DEPFET presents a high
491 signal-to-noise ratio (in 30-50) thanks to the low instrinsic noise and to the large signal
492 achieved with he fully depleted bulk: pixels are thinned to $75 \mu\text{m}$ in the active region,
493 then a MIP is supposed to create a signal of $\sim 6000 e^-$, while the typical noise of DEPFET
494 is around $200 e^-$. **The ASIC read out is still based on a rolling shutter logic, with an**
495 **integration time of 20 μs .** In order to reduce the data-storage memory PXD hits are only
496 used to improve spatial resolution of tracks: the SVD informations are used by the High
497 Level Trigger (HLT) to look for regions of interest in the pixel ladders just by extrapolating
498 back the tracks found in the tracker detector, and this method allows to store only data
499 belonging to these areas; the PXD hits are then used in offline track fit to improve the
500 vertex resolution.

501 MAPS have been proposed for the replacement of VXD during the Long Shut Down
502 2 (LSD2) foreseen around 2026-27; the new vertex detector, VTX, should be made of 5

503 layers fabricated by the optimized Belle II pixel sensor (OBELIX), a detector based on
504 TJ-Monopix have been selected (look at chapter ??). The main advantages VTX should
505 bring are a obvious improving in the track and vertex resolution (14 μm before upgrade,
506 $\lesssim 10 \mu\text{m}$ expected after upgrade) and a reduction in the X_0 (da.. a..), a higher background
507 tolerance because of the smaller sensor than strips dimension and a low bandwidth due to
508 the on-chip sparsification.

509 3.1.2 First attempts to MAPS

510 MIMOSA at EUDET and STAR

511 MIMOSA [6][7] (standing for Minimum Ionizing MOS Active pixel sensor), designed in
512 2008, prefigured the architecture of MAPS for coming vertex detector being the first large
513 scale sensor to be employed as detector. MIMOSA-26 equiped the final version of EUDET
514 high resolution beam telescope both at CERN-SPS and at DESY while the MIMOSA-
515 28 devices are used for the first MAPS-based vertex detector at the STAR experiment.
516 MIMOSA-26 is fabricated in a 350 nm, and a module features 1152 columns, split into
517 18 indipendent groups, and 576 rows, with square pixels having a side of 18.4 μm lenght;
518 therefore, beacuse of the small dimension, charge sharing is an issue aggiungi qualcosa.
519 The readout is done in a rolling shutter mode: the chip is an Active Pixels (APS) and
520 therefore it incorporates the amplification on pixel, while the signal discrimination and
521 zero-suppression logic are placed at the EoC, where is also placed a memory. The chip
522 is an Active Pixels (APS) and therefore it incorporates the amplification on pixel, while
523 the signal discrimination and zero-suppression logic are placed at the EoC: the readout is
524 done in a rolling shutter mode with a frame integration time that can be lowered down to
525 85 ms, and a memory allowing to store up to six hits is.

526 The EUDET telescope, equipped with six sensor planes, requires highly granular and
527 thin pixel detectors in order to achieve an excellent track resolution (around 2 μm) even at
528 the rather low particle energies of up to 6 GeV. The STAR experiment at the Relativistic
529 Heavy Ion Collide (RHIC) accelerator at the Brookhaven National Laboratory (BNL) is
530 the first to include MAPS in the vertex detector[8]. The main tracking detector in STAR is
531 a TPC with radii 60-190 cm embedded in a 0.5 T solenoidal magnetic field, that provides
532 a pointing resolution of approximately 1 mm. The pixel detector, PXL, is a part of a
533 3-detector system, Heavy Flavor Tracker (HFT), that has been added to the pre-existing
534 STAR apparatus just before the 2014 Run in order to improve the impact parameter
535 resolution and to enable the direct reconstruction of hadronic decays of heavy flavor mesons
536 and baryons. The Heavy Flavor Tracker (HFT) is composed by the Silicon Strip Detector
537 (SSD), the Intermediate Silicon Tracker (IST) and the Pixel Detector (PXL); the first
538 one is placed at 22 cm from the beam pipe and consists of double sided strips with 95 μm
539 inter-strip pitch, the second one, placed at 14 cm, is made of single sided silicon pads
540 with $600 \mu\text{m} \times 6 \text{ mm}$ pitch and the last one made by two layes is placed at 2.8 cm and 8 cm
541 fabricated with ULTIMATE2 (also known as MIMOSA-28), a successor of MIMOSA-26
542 sensor, with pitch 20.7 μm and thinned down to 50 μm . An area of 0.16 m^2 are covered
543 by 400 MAPS sensor, corresponding to 356 milions of pixels divided into array size of 928
544 \times 960. Each pixel includes circuitry for readout, amplification, and Correlated Double
545 Sampling (CDS) for signal extraction and noise subtraction and the frame integration time
546 is $185.6 \mu\text{s}$; after the subtraction the signal to noise ratio is ~ 30 , with a noise between
547 10-12 electrons and a signal of 1000 e^- . Thanks to the HFT system and the PXL, STAR

548 achieved a track pointing resolution $46 \mu\text{m}$ for $750 \text{ MeV}/c$ kaons, and better than $30 \mu\text{m}$ for
 549 particle momenta bigger than $1 \text{ GeV}/c$: this performance enabled the study of D-meson
 production with a high significance signal.

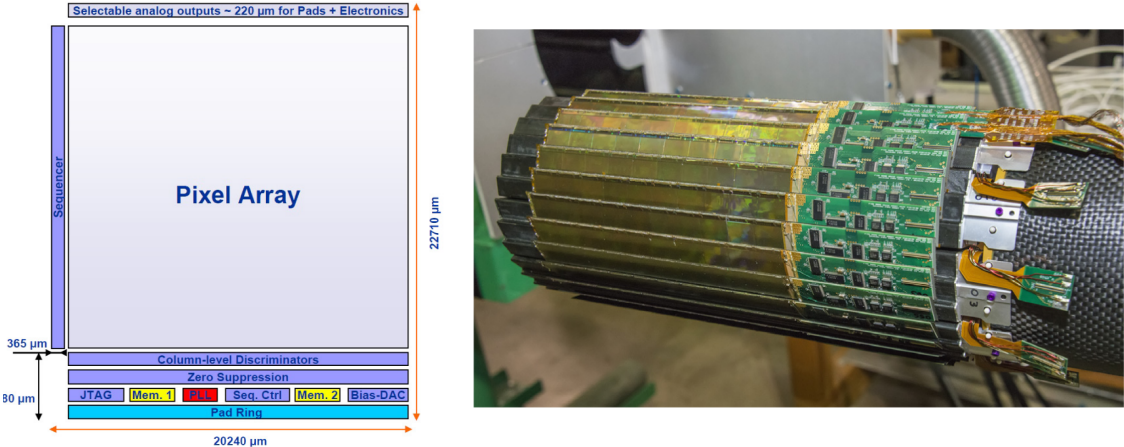


Figure 3.1: (a) The HFT PXL detector; (b) Block-diagram of the ULTIMATE-2 sensor

550

551 ALPIDE at ALICE

552 ALICE (A Large Ion Collider Experiment) is a detector dedicated to heavy-ion physics
 553 and to the study of the condensed phase of the chromodynamics at the LHC. The tracking
 554 detector consists of the Inner Tracking System (ITS), the gaseous Time Projection Cham-
 555 ber (TPC) and the Transition Radiation Detector (TRD), and all those are embedded in
 556 a magnetic field of 0.5 T . The ITS is made by six layers of detectors, two for each type,
 557 from the interaction point outwards: Silicon Pixel Detector (SPD), Silicon Drift Detector
 558 (SDD) and Silicon Strip Detector (SSD). Contrary to the others LHC experiments, AL-
 559 ICE tracker is placed in a quite different environments: the expected dose is smaller by
 560 two order of magnitude and the rate of interactions is few MHz instead of 40 MHz, but
 561 the number of particles comes out of each interaction is higher (the SPS is invested by a
 562 density of particles of $\sim 100 \text{ cm}^{-2}$). The reconstruction of very complicated events with a
 563 large number of particles is a challenge, hence to segment and to minimize the amount of
 564 material, which may cause secondary interaction complicating further the event topology, is
 565 considered a viable strategy. The detector employs the ALPIDE chip, developed by AL-
 566 ICE collaboration, fabricated in the 180 nm CMOS Imaging Sensor process of TowerJazz,
 567 whose design takes full advantage of process feature which allows full circuitry within the
 568 pixel matrix. Thanks to the reduction of the material budget, ITS2 obtained an amazing
 569 improvement both in the position measurement and in the momentum resolution, improv-
 570 ing the efficiency of track reconstruction for particles with very low transverse momentum
 571 (by a factor 6 at $pT \sim 0.1 \text{ GeV}/c$). Further advancements in CMOS MAPS technology
 572 are being aggressively pursued for the ALICE ITS3 vertex detector upgrades (foreseen
 573 around 2026-27), with the goals of further reducing the sensor thickness and improving
 574 the readout speed of the devices, while keeping power consumption at a minimum.

575 3.2 Other applications

576 Historically for imaging purpose the CCDs were the favoured device: they can be used as
577 single photon counter or integrating and collecting the charge released by more impinging
578 particles. The utilisation in the first case is similar to the tracking one, except that the
579 requirements are less tight, so much that two noteworthy of microchips originally meant for
580 detectors in particle physics at the LHC, and later employed in other fields are Medipix
581 and Timepix. They are read-out chips developed by the Medipix Collaborations since
582 early 1990s. For two decades, different Medipix generations have been produced, having
583 a rough correlation with the feature size used: Medipix2 (1999) used 250 nm feature size
584 CMOS while Medipix3 (2005) 130 nm. The aim of the fourth collaboration (2016), instead,
585 is designing pixel read-out chips that prepared for **TSV processing and may be tiled on**
586 **all four sides. DOVREI METTERE DUE RIGHE SU TSV OPPURE TAGLIARE.** For
587 photons imaging other materials with higher atomic charge than silicon could be prefered,
588 as a high photon absorption efficiency is needed: it was for this reason that Medipix2 was
589 bump bonded to identically segmented sensors of both silicon and GaAs.

590 The applications in scientific imaging vary from astrophysics and medical imaging to
591 more exotic domains as studies of protein dynamics, art authentication and dosimetry. The
592 most important employment of Medipix is as X-ray single photon counting in industrial
593 and medical radiography and in 3D computed tomography. Thanks to a New-Zealand
594 company, the MARS Bioimaging detector has been fabricated, which is capable of resolving
595 the photons energy and produce 3D coloured images. Besides tracking in HEP (I have
596 already cited the use of Timepix3 is in the beam telescope of the LHCb VELO), an
597 important use of Timepix is in dosimetry **Timepix Detector for Imaging in Ion Beam**
598 **Radiotherapy- aggiungi qualche info** A small-Timepix detector with the dimension of a
599 USB can also be found at the International Space Station, where it is exploited for radiation,
600 principally made of heavy-ion, monitoring.

601 3.2.1 Applicability to FLASH radiotherapy

602 A possible new application of pixels detector is dosimetry or beam monitoring of charged
603 particles in high intensity radiography. The radiological treatment is a common method
604 used in 60% of tumors both as palliative care and as treatment. It can be given before,
605 after or during a surgery, (Intra operative radiation therapy-IORT) and many different
606 types of radiations (photons, electrons, protons and ions, which mainly are hydrogen and
607 carbon) can be used to irradiate the affected tissues. Exploiting the ionizing energy loss,
608 that can be parametrized by the Linear Energy Transfer (LET), a biological damage can
609 be delivered to the tissue: while α and β particles are high LET radiations with values in
610 100 keV/ μ m to 200 keV/ μ m, x-rays and gamma-rays are low LET radiations with values in
611 range 0.2 keV/ μ m to 2 keV/ μ m.

612 If x-ray photons, with energy in 4 MeV to 25 MeV are used, the ionization is caused
613 by the Compton electrons and is more in the superficial layers of the tissue due to the
614 exponential attenuation of the beam. The hadrons energy loss, instead, is strongly lo-
615 calized in the last region of the track, that is the Bragg peak. Ion beam enables better
616 focusing of the radiation thereby improves the sparing of the surrounding healthy tissues;
617 on the other hand the delivered dose distribution depends more on the patient's density
618 tissues (e.g. bones, swelling, fat). **Ensuring the target coverage is a fundamental objective**
619 **in radiotherapy and is closely connected to the choice of the particles. Electrons cover the**

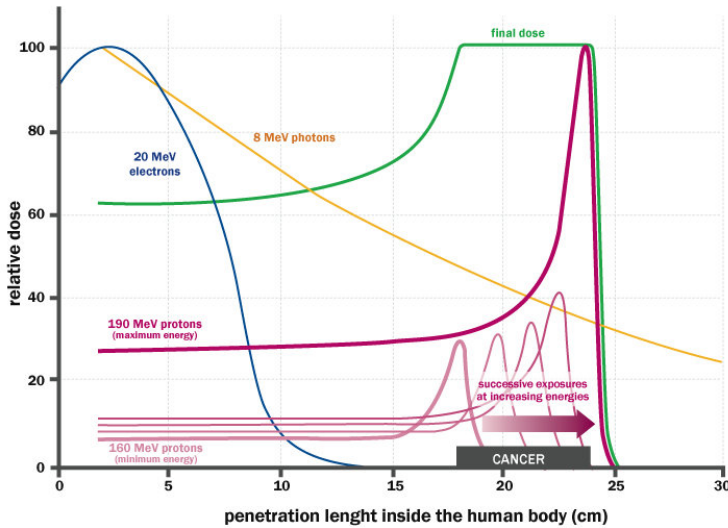


Figure 3.2: The Spread Out Bragg Peak (SOBP) curve (green), which is a constant dose distribution, is obtained from the superposition of many Bragg peak of hadrons with different energy.

	CONV-RT	FLASH-RT
Dose rate	0.03 Gy/s	40 Gy/s
Intra pulse dose rate	100 Gy/s	106 Gy/s
Treatment duration	~minutes	\lesssim 500 ms
DDP	0.3 mGy	1 Gy to 10 Gy
Pulse width	3 μ s	\sim 2 μ s

Table 3.1: Typical value of treatment parameters

target since they tend to spread out and can cover a field size of a few cm^2 at a distance of a few cm from the source. Instead, the limited size of the beam for protons and photons from ultra high dose rate microbeam radiation therapy (MRT), for which FLASH effect was seen, requires the scanning of target. The radiobiological consequences of scanning both in spatial-fractionation and in prolonged exposure, which might not be sufficient to maintain a high mean dose rate to trigger FLASH effect, need to be explored. To date, the FLASH effect has been most commonly demonstrated using low-energy electron linacs

Recently² a promising method for RT at ultra high dose rate (at least 40 Gy/s) and for this reason called FLASH-RT[9], instead of CONV-RT (0.03 Gy/s), came out. This treatment takes advantages of biological differences between tumors and healthy tissues: it is characterized by reducing normal tissue toxicity and maintaining equivalent tumor damage. The response to dose can be described by the survival fraction probability, describing the fraction of surviving cell as a function of the dose:

$$S(D) = S(0) e^{-(\alpha D + \beta D^2)} \quad (3.1)$$

²The first evidences has been observed on a mice experiments in 1966 and in 2014 by the group of Favaudon and Vozenin. After this, many test on cats and pigs have been performed, and also there has been a clinical trial on a cutaneous tumor-patient

633 where α and β respectively represents the rate of cell killing by single ionizing events and
 634 by double hits. Hence, at high doses the density of damages increases and the cells repair
 635 becomes more difficult. Even if the FLASH effect is not yet completely understood and
 636 the underlying mechanisms are not clear, it looks like there are two different recipes which
 637 are involved:

- 638 • **The dose rate:** higher dose rate produce bigger damages (fig. 3.3(a)) since this
 639 prevent cells from sparing.
- 640 • **The presence or absence of oxygen:** while hypoxic cells are very resistant to radi-
 641 ation, normal oxygenated cells are highly radiosensitive. This is because if molecules
 642 containing O_2 break due to the impinging radiation, then the oxygen can build Re-
 643 active Oxygen Species (ROS) (fig.3.3(b))

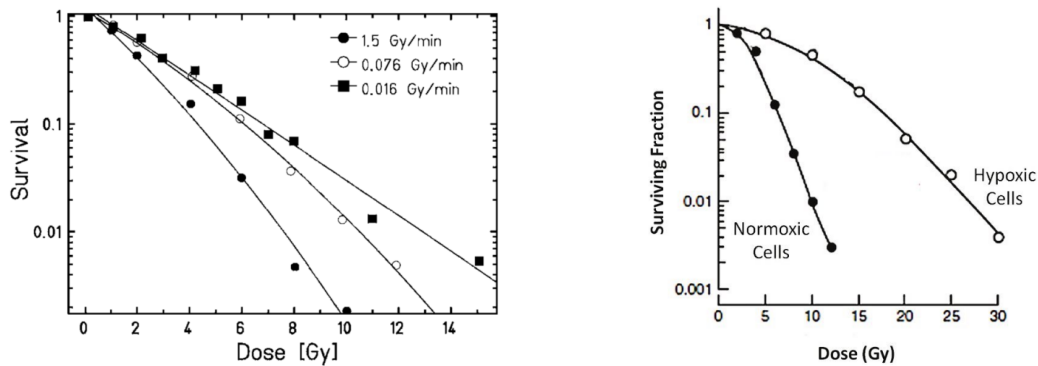


Figure 3.3: (a) Survival curve for different dose rate and (b) for different oxygen cell content

644 The Tumor Control Probability (TCP) and the Normal Tissue Complication (NTC)
 645 functions parametrize respectively the efficiency of damaging on the tumor after having
 646 released a certain dose and the probability of not affecting the healthy tissues. The
 647 intermediate zone between the increase of the TC and of the NTC is called therapeutic
 648 window, and the wider it is and the more effective the treatment is.

649 Dosimetric problems

650 Finding dosimeters suitable for online monitoring of the beam at ultra high dose rate is
 651 still an open issue since almost all standard online dosimeters show saturation problems.
 652 Differently, radiochromic films, which are the standard passive dosimeters, show dose-rate
 653 indipendence up to 109 Gy/s. **Cosa sono i radiochromic films and they do not have the same**
 654 **accuracy of other detectors.** The principal detectors for reference dosimetry which provide
 655 real-time dose measurement are Ionization Chambers (IC), that show saturation issue at
 656 dose per pulse (DDP) two orders of magnitude lower than the ones used for FLASH-RT.
 657 **da qui in poi** ICs devono essere calibrate secondo la metrologia , per cui grazie a protocolli
 658 di calibrazione e introducendo dei fattori correttivi si riesce a fare una misura di dose.
 659 k_{sat} which accounts for the loss of charge collected due to recombination. Doppi problemi
 660 sia di saturazione dovuta a ion recombination sia di scariche, must be carefully accounted
 661 for: questo doppio effetto è dato dal fatto che, creandosi tante cariche nella camera, che
 662 va ad annullare il campo elettrico di drift. Questo ovviamente paralizza le cariche che non

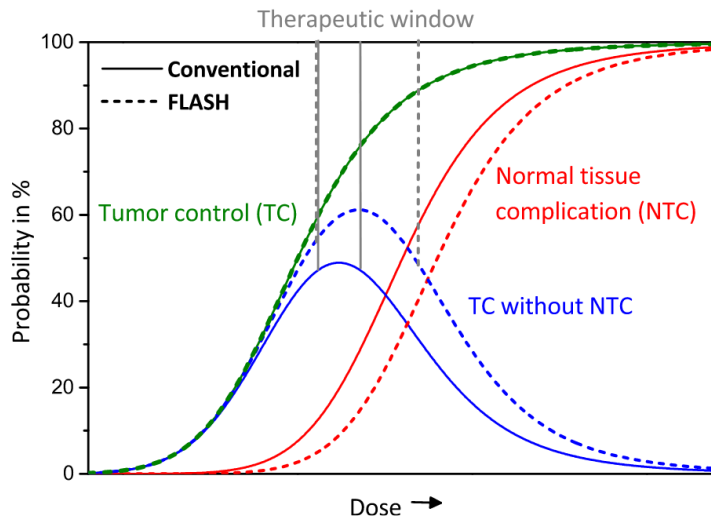


Figure 3.4: Illustration of dependence of TCP, NTCP and therapeutic window on dose, for CONV-RT ad FLASH-RT.

663 driftano più, ma che anzi si ricombinano ed inoltre facilita la formazione di scariche. Per
 664 DDP minori di 1 mGy il fattore correttivo è minore al 5%, poi però aumenta substantially.

665 Scintillators have reusable, non-exhaustible scintillation centers. However, the system
 666 has a total deadtime given by both the crystal scintillation time and the electronics read-
 667 out deadtime.

668 Semiconductors show a nonreversible saturation beyond a threshold around 15 cGy/p.
 669 The scintillator used, shows a negligible saturation up to 1 Gy/p, but it increases signifi-
 670 cantly up to at least 11 Gy/p, and it reaches a cutoff value between 11 and 36 Gy/p.

671 Scintillator dosimeters are widely used in radiotherapy. They are usually operating in
 672 counting-mode where each detected signal is processed by read-out electronics. However,
 673 the system has a total deadtime given by both the crystal scintillation time and the
 674 electronics read-out deadtime When a scintillator dosimeter is used in integrator-mode
 675 the signal is integrated over the entire irradiation time.A deadtime, due to the decay time
 676 of the scintillating material, is considered on average every N recorded pulses, where N is
 677 the number of scintillation centres in the dosimeter.

678 Besides saturation two other requirements for online dosimeters are high temporal and
 679 space resolutions. Si potrebbe pensare di poter usare i pixel detector as beam monitor
 680 che hanno risoluzioni spaziali anche inferiori al 10 um e ris temporali -qua dare un valore
 681 è più difficile perchè per i maps la risoluzione temporale dipende da l occupancy. Uno dei
 682 problemi è però il lungo dead time introdotto dal lungo tempo di readout (ricordiamo
 683 che sopportano circa 100 Mhz/cm²).

684 **Chapter 4**

685 **TJ-Monopix1**

686 TJ-Monopix1 is a small electrode DMAPS with fast R/O capability, fabricated by Tow-
 687 erJazz foundry in 180 nm CMOS imaging process. It is part, together with prototypes
 688 from other series such as TJ-MALTA, of the ongoing R&D efforts aimed at developing
 689 DMAPS in commercial CMOS processes, that could cope with the requirements at ac-
 690 celerator experiments. Both TJ-Monopix and TJ-MALTA series [10], produced with the
 691 same technology by TowerJazz (the timeline of the foundry products is shown in figure
 692 4.1), are small electrode demonstrators and principally differ in the readout design: while
 693 Monopix implements a column-drain R/O, an asynchronous R/O without any distribution
 694 of BCID has been used by TJ-Malta in order to reduce power consumption.



Figure 4.1: Timeline in TowerJazz productions in 180 nm CMOS imaging process

695 Another Monopix series, but in 150 nm CMOS technology, has been produced by
 696 LFoundry [11]. The main differences between the LF-Monopix1 and the TJ-Monopix1
 697 (summarized in table 4.2), lay in the sensor rather than in the readout architecture, as
 698 both chips implements a fast column drain R/O with ToT capability [12][13]. Concerning
 699 the sensors, either are based on a p-type substrate, but with slightly different resistivities;
 700 in addition LFoundry pixels are larger, thicker and have a large fill factor (the very deep n-
 701 well covers ~55% of the pixel area). The primary consequence is that LF-Monopix1 pixels
 702 have a higher capacity resulting in higher consumption and noise. As I discussed in section
 703 2.4.1, the fact that LF-Monopix has a large fill factor electrode is expected to improve its
 704 radiation hardness. Indeed, a comparison of the performance of the two chips showed that
 705 TJ-Monopix suffers a comparatively larger degradation of efficiency after irradiation, due
 706 to the low electric field in the pixel corner; on the other hand, a drawback of the large fill
 707 factor in LF-Monopix is a significant cross-talk.

	LF-Monopix1	TJ-Monopix1
Resistivity	$>2 \text{ k}\Omega\text{cm}$	$>1 \text{ k}\Omega\text{cm}$
Pixel size	$50 \times 250 \mu\text{m}^2$	$36 \times 40 \mu\text{m}^2$
Depth	$100\text{-}750 \mu\text{m}$	$25 \mu\text{m}$
Capacity	$\sim 400 \text{ fF}$	$\sim 3 \text{ fF}$
Preamplifier	charge	voltage
Threshold trimming	on pixel (4-bit DAC)	global threshold
ToT	8 bits	6 bits
Consumption	$\sim 300 \text{ mW/cm}^2$	$\sim 120 \text{ mW/cm}^2$
Threshold	$1500 e^-$	$\sim 270 e^-$
ENC	$100 e^-$	$\sim 30 e^-$

Table 4.1: Main characteristics of Monopix1 produced by TowerJazz and LFoundry [12][13]

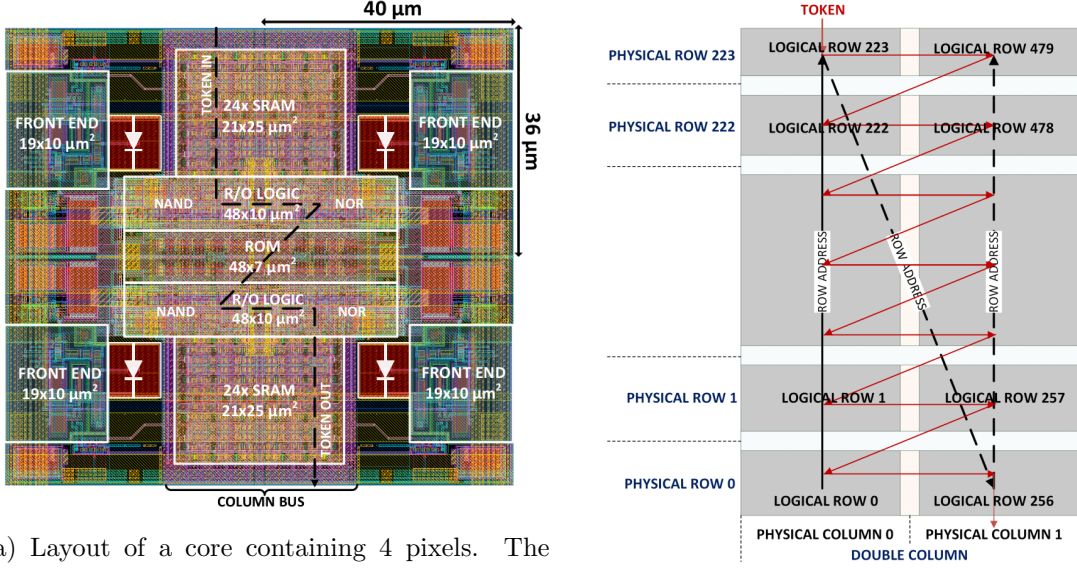
708 The TJ-Monopix1 chip contains, apart from the pixels matrix, all the required support
 709 blocks used for configuration and testing:

- 710 • the whole matrix contains 224×448 pixels, yielding a total active area approximately
 711 equal to 145 mm^2 over a total area of $1 \times 2 \text{ cm}^2$;
- 712 • at the chip periphery are placed some 7-bit Digital to Analog Converter (DAC), used
 713 to generate the analog bias voltage and current levels and to configugre the FE;
- 714 • at the EoC is placed a serializer to transferred datas immediately, indeed no trigger
 715 memory is implemented in this prototypes;
- 716 • the matrix power pads are distributed at the sides
- 717 • four pixels which have analog output and which can be monitored with an oscillo-
 718 scope, and therefore used for testing

719 Pixels are grouped in 2×2 cores (fig. 4.2a): this layout allows to separate the analog
 720 and the digital electronics area in order to reduce the possible interference between the
 721 two parts. In addition it semplifies the routing of data as pixels on double column share
 722 the same column-bus to EoC. Therefore pixels can be addressed through the physical
 723 column/row or through the logical column/row, as shown in fig. 4.2b: in figure is also
 724 highlighted the token propagaion path, whose I will discuss later.

725 4.1 The sensor

726 As already anticipated, TJ-Monopix1 has a p-type epitaxial layer and a n doped small
 727 collection electrode ($2 \mu\text{m}$ in diameter); to avoid the n-wells housing the PMOS transistors
 728 competing for the charge collection, a deep p-well substrate, common to all the pixel FE
 729 area, is used. TJ-Monopix1 adopts the modification described in section 2.4.2 that allows
 730 to achieve a planar depletion region near the electrode applying a relatively small reverse
 731 bias voltage. This modification improves the efficiency of the detector, especially after
 732 irradiation, however a simulation of the electric field in the sensor, made with the software
 733 TCAD (Technology Computer Aided Design), shows that a nonuniform field is still pro-
 734 duced in the lateral regions of the pixel compromising the efficiency at the corner. Two



(a) Layout of a core containing 4 pixels. The analog FE and the digital part are separated in order to reduce cross-talk be

(b)

Parameter	Value
Matrix size	$1 \times 2 \text{ cm}^2$
Pixel size	$36 \times 40 \mu\text{m}^2$
Depth	$25 \mu\text{m}$
Electrode size	$2 \mu\text{m}$
BCID	40 MHz
ToT-bit	6
Power consumption	$\sim 120 \text{ mW/cm}^2$

Table 4.2

variations to the process have been proposed in order to further enhance the transversal component of electric field at the pixel borders: on a sample of chip, which includes the one in Pisa, a portion of low dose implant has been removed, creating a step discontinuity in the deep p-well corner (fig. 4.3); the second solution proposed[MOUSTAKAS THESY, PAG 58] consists in adding an extra deep p-well near the pixel edge. A side effect of the alteration in the low dose implant is that the separation between the deep p-well and the p-substrate becomes weak to the point that they cannot be biased separately to prevent the punchthrough.

Moreover, to investigate the charge collection properties, pixels within the matrix are split between bottom top half and bottom half and feature a variation in the coverage of the deep p-well: the electronics area can be fully covered or not. In particular the pixels belonging to rows from 0 to 111 are fully covered (FDPW) and pixels belonging to rows from 112 to 223 have a reduced p-well (RDPW), resulting in a enhancement of the lateral component of the electric field.

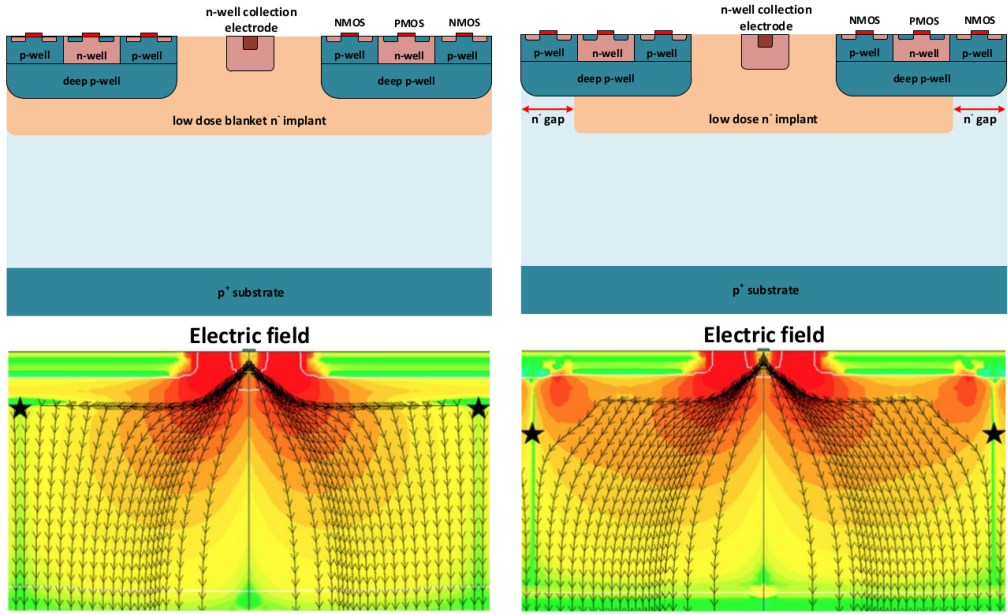


Figure 4.3: (a) The cross-section of a monolithic pixel in the TJ-Monopix with modified process; additionally in (b) a gap in the low dose implant is created to improve the collection of charge due to a bigger lateral component of the electric field. this point in figure is indicated by a star . transversal component of the electric field drops at the pixel corner

749 4.2 Front end

750 The matrix is split in four sections, each one corresponding to a different flavor of the FE.
 751 The four variation have been implemented in order to test the data-bus readout circuits
 and the input reset modes.

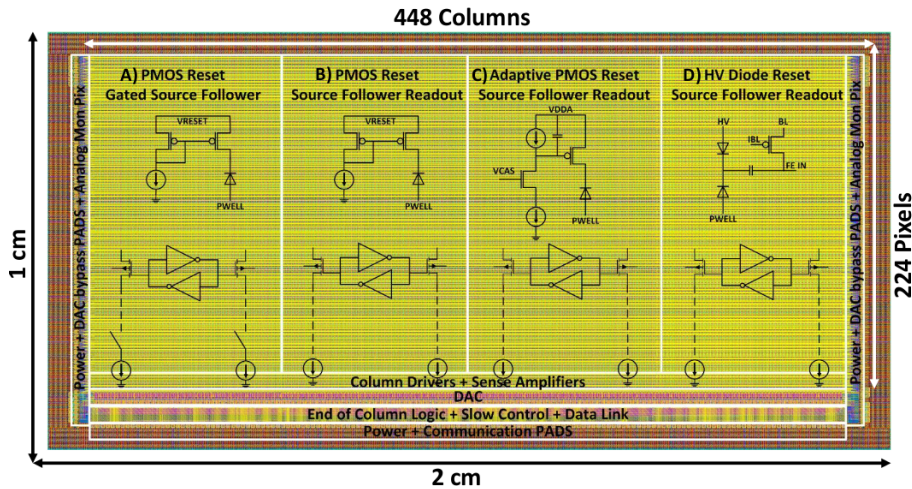


Figure 4.4

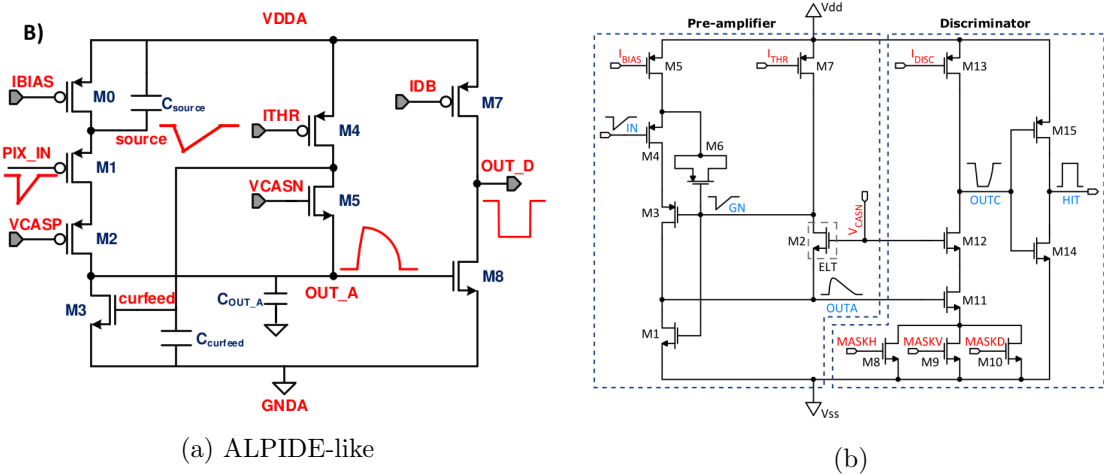
752 All the flavors implement a source-follower double-column bus readout: the standard
 753 variation is the flavor B, that features a PMOS input reset (refered as "PMOS reset").
 754 Flavor A is identical to flavor B except for the realization of the source follower (it is a
 755 gated one) that aim to reduce the power consumption.**cosa significa?** C instead implements

757 a novel leakage compensation circuit. Moreover the collection electrode in flavors A, B, C
 758 is DC-coupled to the front-end input, while in D is AC-coupled, providing to applu a high
 759 bias voltage; for this reason flavor D il called "HV flavor".

760 Principio generale: R resistenza di reset deve essere abbastanza grande in modo da
 761 far si che il ritorno allo zero è abbastanza lento (non devi "interferire" con la tot slope e
 762 non deve essere più corto del tempo del preamplificatore, sennò hai perdita di segnale).
 763 Baseline reset: all'input solitamente hai un PMOSS o un diodo; R reset

764 4.2.1 ALPIDE-like

765 ALPIDE chips, developed by the ALICE collaboration, implemented a standard FE to the
 766 point that many CMOS MAPS detectors used a similar FE and are called "ALIPDE-like".
 767 Considering that both TJ-Monopix1 and ARCADIA-MD1 have an ALPIDE-like FE, I am
 going to explain the broad principles of the early FE stage. The general idea is of the



768
 769 amplification to transfer the charge from a bigger capacity[14], C_{source} , to a smaller one,
 770 C_{out} : the input transistor M1 with current source IBIAS acts as a source follower and this
 771 forces the source of M1 to be equal to the gate input $\Delta V_{PIX_IN} = Q_{IN}/C_{IN}$.

$$Q_{source} = C_{source} \Delta V_{PIX_IN} \quad (4.1)$$

772 The current in M2 and the charge accumulates on C_{out} is fixed by the one on C_{source} :

$$\Delta V_{OUT_A} = \frac{Q_{source}}{C_{OUT_A}} = \frac{C_{source} \Delta V_{PIX_IN}}{C_{OUT_A}} = \frac{C_{Source}}{C_{OUT_A}} \frac{Q_{IN}}{C_{IN}} \quad (4.2)$$

773 A second branch (M4, M5) is used to generate a low frequency feedback, where VCASN
 774 and ITHR set the baseline value of the signal on C_{OUT_A} and the velocity to goes down
 775 to the baseline.

776 IL RUOLO DI CURVFEED NON L'HO CAPITO.

777 Finally IDB defines the charge threshold with which the signal OUT_A must be compared:
 778 depending on if the signal is higher than the threshold or not, the OUT_D is high or low
 779 respectively.

780 The actual circuit implemented in TJ-Monopix1 is shown in figure 4.5b: the principal
 781 difference lays in the addition of disableing pixels' readout. This possibility is uttermost
 782 important in order to reduce the hit rate and to avoid saturating the bandwidth due to the

Parameter	Meaning	
IBIAS	mainly controls the rise time	yes? check
IDB	sets the discriminator threshold	yes
ITHR	sets the velocity of the return to the baseline	yes
ICASN	sets the baseline of the signal	yes
VRESET	sets the gain of the preamplifier	yes
IRESET	sets the gain of the preamplifier	no

Table 4.3: FE parameters which must be setted through the DAQ. "Function" means that higher parameter implies higher value

783 noisy pixels, which typically are those with manufacturing defects. In the circuit transis-
 784 tors M8, M9 and M10 have the function of disabling registers with coordinates MASKH,
 785 MASKV and MASKD (respectively vertical, orizontal and diagonal) from readout: if all
 786 three transistors-signals are low, the pixel's discriminator is disabled. Compared with a
 787 configurable masking register which would allow disableing pixels individually, to use a
 788 triple redundancy reduces the sensistivity to SEU but also gives amount of intentionally
 789 masked ("ghost") pixels. This approach is suitable only for extremely small number N of
 790 pixel has to be masked: if two coordinate projection scheme had been implemented, the
 791 number of ghost pixels would have scale with N^2 , if instead three coordinates are used,
 the N's exponential is lower than 2 (fig. 4.6)

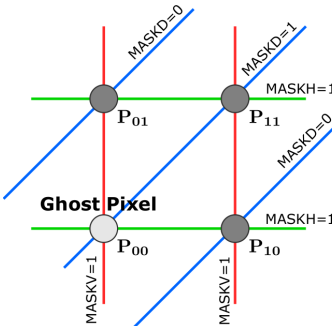


Figure 4.6

792

793 4.3 Readout logic

794 TJ-Monopix1 has a triggerless, fast and with ToT capability R/O which is based on a
 795 column-drain architecture. On the pixel are located two Random Access Memory (RAM)
 796 cells to store the 6-bit LE and 6-bit TE of the pulse, and a Read-Only Memory (ROM)
 797 containing the 9-bit pixel address. Excluded these memories, TJ-Monopix1 hasn't any
 798 other buffer: if a hit arrives while the pixel is already storing a previous one, the new
 799 data get lost. After being read, the data packet is sent to the EoC periphery of the
 800 matrix, where a serializer transfers it off-chip to an FPGA (4.7). There a FIFO is used
 801 to temporarily stored the data, which is transmitted to a computer through an ethernet
 802 cable in a later time.

803 The access to the pixels' memory and the transmission of the data to the EoC, following

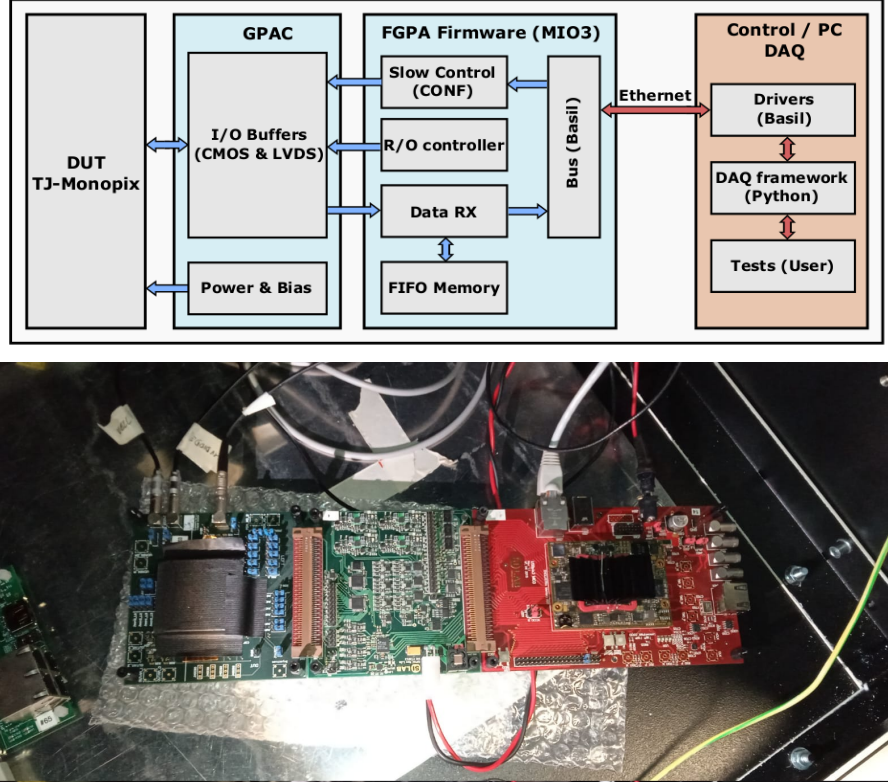
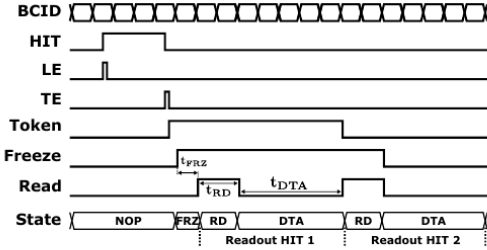


Figure 4.7: Main caption

a priority chain, is managed by control signals and is based on a Finite State Machine (FSM) composed by four state: no-operation (NOP), freeze (FRZ), read (RD) and data transfer (DTA). The readout sequence (??) starts with the TE of a pulse: the pixel immediately tries to grab the column-bus turning up a hit flag signal called *token*. The token is used to control the priority chain and propagates across the column indicating what pixel that must be read. To start the readout and avoid that the arrival of new hits disrupt the priority logic, a *freeze* signal is activated, and then a *read* signal controls the readout and the access to memory. During the freeze, the state of the token for all pixels on the matrix remains settled: this does not forbid new hits on other pixels from being recorded, but forbids pixels hit from turning on the token until the freeze is ended. The freeze stays on until the token covers the whole priority chain and gets the EoC: during that time new token cannot be turned on, and all hits arrived during a freeze will turn on their token at the end of the previous freeze. Since the start of the token is used to assign a timestamp to the hit, the token time has a direct impact on the time resolution measurement; this could be a problem coping with high hits rate.

The analog FE circuit and the pixel control logic are connected by an edge detector which is used to determine the LE and the TE of the hit pulse(figure 4.9): when the TE is stored in the first latch the edge detector is disabled and, if the **FREEZE** signal is not set yet, the readout starts. At this point the HIT flag is set in a second latch and a token signal is produced and depending on the value of **Token in** the pixel can be read or must wait until the **Token in** is off. In figure an OR is used to manage the token propagation, but since a native OR logic port cannot be implemented with CMOS logic, a sum of a NOR and of an inverter is actually used; this construct significantly increases the propagation



(b) Readout sequence timing diagram. In this example two hits are being processed.

Figure 4.8: Readout timing diagram: in this example two hits are being processed

delay (the timing dispersion along a column of 0.1-0.2 ns) of the token and to speed up the circuit optimized solution are often implemented. When the pixel become the next to be read in the queue, and at the rising edge of the **READ** signal, the state of the pixel is stored in a D-latch and the pixel is allowed to use the data bus; the TE and the HIT flag latches are reset and a **READINT** signal that enable access of the RAM and ROM cells is produced.

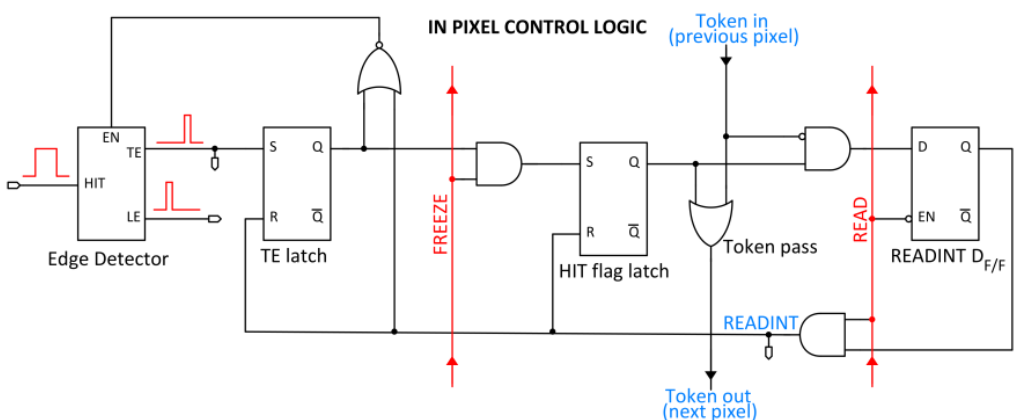


Figure 4.9

The final data must provide all the hits' information: the pixel address, the ToT and the timestamp. All those parts are assigned and appended at different time during the R/O chain:

- **Pixel address:** while the double column address (6-bit) is appended by the EoC circuit, the row address (8-bits for each flavor) and the physical column in the doublet (1-bit) are assigned by the in-pixel logic
- **ToT:** is obtained offline from the difference of 6-bits TE and 6-bits LE, stored by the edge detector in-pixel; since a 40 MHz BCID is distributed across the matrix, the ToT value is range 0-64 clock cycle which corresponds to 0-1.6 μ s
- **Timestamp:** The timestamp of the hit correspond to the time when the pixel set up the token; it is assigned by the FPGA, that uses the LE, TE and a 640 MHz clock to derive it. For all those hits which arrived while the matrix is frozen, the timestamp is no more correlated with the time of arrival of the particle

When the bits are joined up together the complete hit data packet is 27-bit.

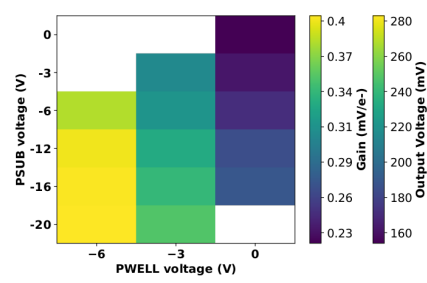


Figure 4.10: 2D map of the output voltage amplitude and gain with respect to the p-well and p-substrate in the case of the PMOS reset front-end

848 **Chapter 5**

849 **Arcadia-MD1**

850 [15] [16]

851 Breve introduzione analoga a Monopix1 in cui descrivo brevemente la "timeline" da
852 SEED Matisse a Md1 e Md2

853 **5.1 The sensor**

854 ARCADIA-MD1 is an LFoundry chip which implements the technology 110 nm CMOSS
855 node with six metal layer ???. The standard p-type substrate was replaced with an n-type
856 floating zone material, that is a tecnique to produce purified silicon crystal. (pag 299
857 K.W.).

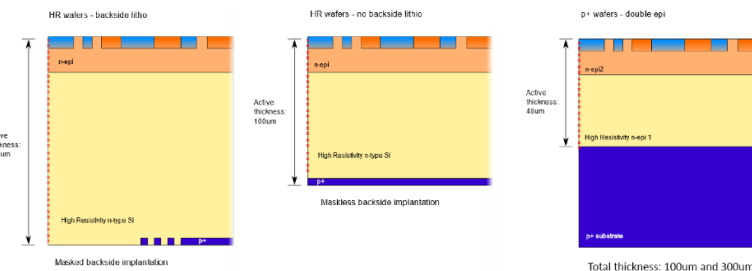


Figure 5.1

858

859 Wafer thinning and backside lithography were necessary to introduce a junction at the
860 bottom surface, used to bias the substrate to full depletion while maintaining a low voltage
861 at the front side.

862 C'è un deep pwell per - priority chainseparare l'elettronica dal sensore; per controllare il
863 punchthrough è stato aggiunto un n doped epitaxial layer having a resistivity lower than
864 the substrate.

865 RILEGGI SUL KOLANOSKY COS'È IL PUNCHTHROUGH, FLOAT ZONE MA-
866 TERIAL, COME VENGONO FATTI I MAPS COME FAI LE GIUNZIONI

867 It is part of the cathegory of DMAPS Small electrode to enhance the signal to noise
868 ratio.

869 It is operated in full depletion with fast charge collection by drift.

870 Prima SEED si occupa di studiare le prestazioni: oncept study with small-scale test

871 structure (SEED), dopo arcadia: technology demonstration with large area sensors Small
 872 scale demo SEED(sensor with embedded electronic developement) Quanto spazio dato
 873 all'elettronica sopra il pwell e quanto al diodo. ..

874 5.2 Readout logic and data structure

875 5.2.1 Matrix division and data-packets

876 The matrix is divided into an internal physical and logical hierarchy: The 512 columns are
 877 divided in 16 section: each section has different voltage-bias + serializzatori. Each section
 878 is devided in cores () in modo che in ogni doppia colonna ci siano 1Pacchetto dei dati 6
 879 cores. ricordati dei serializzaatori: sono 16 ma possono essere ridotti ad uno in modalità
 spazio

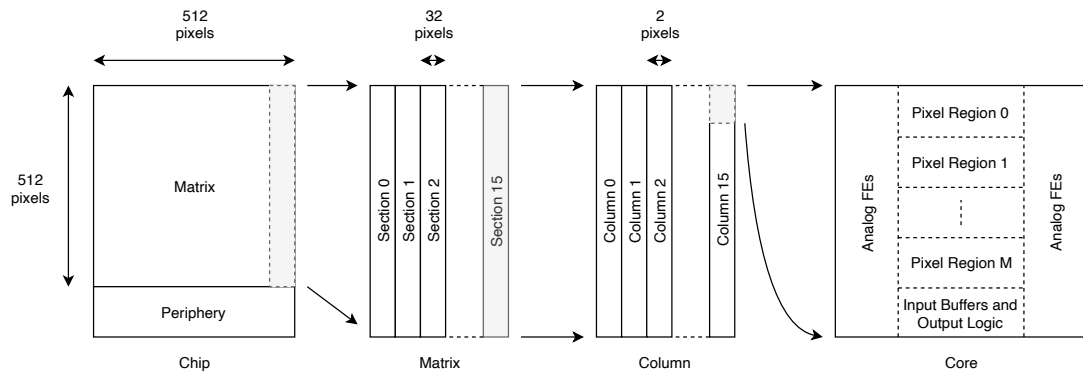


Figure 5.2

880

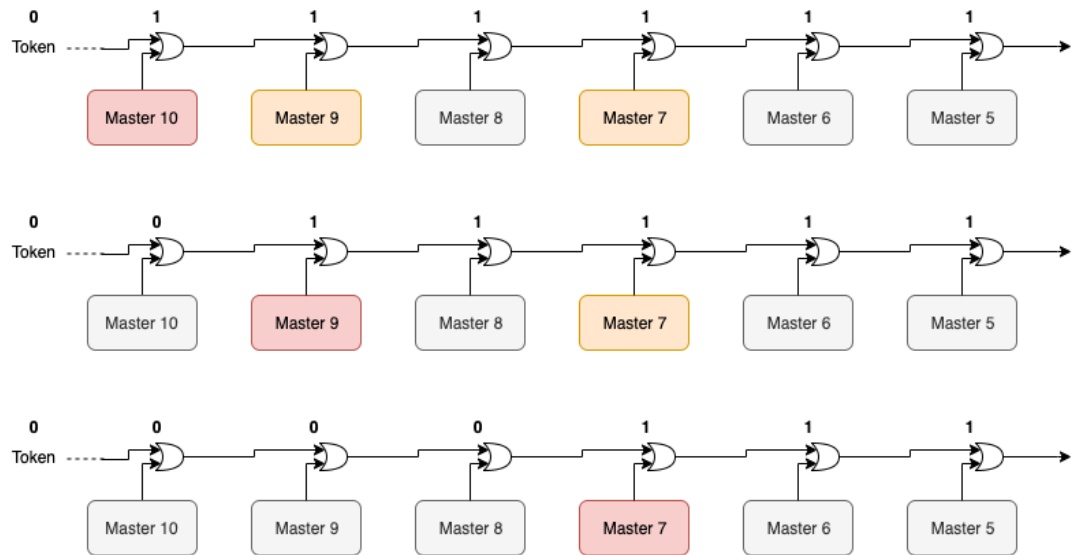


Figure 5.3

881 Questa divisione si rispecchia in come sono fatti i dati: scrivi da quanti bit un dato è
 882 fatto e le varie coordinate che ci si trovano dentro; devi dire che c'è un pixel hot e spieghi
 883 dopo a cosa serve, e devi accennare al timestamp

884 "A core is simply the smallest stepped and repeated instance of digital circuitry. A
 885 relatively large core allows one to take full advantage of digital synthesis tools to imple-

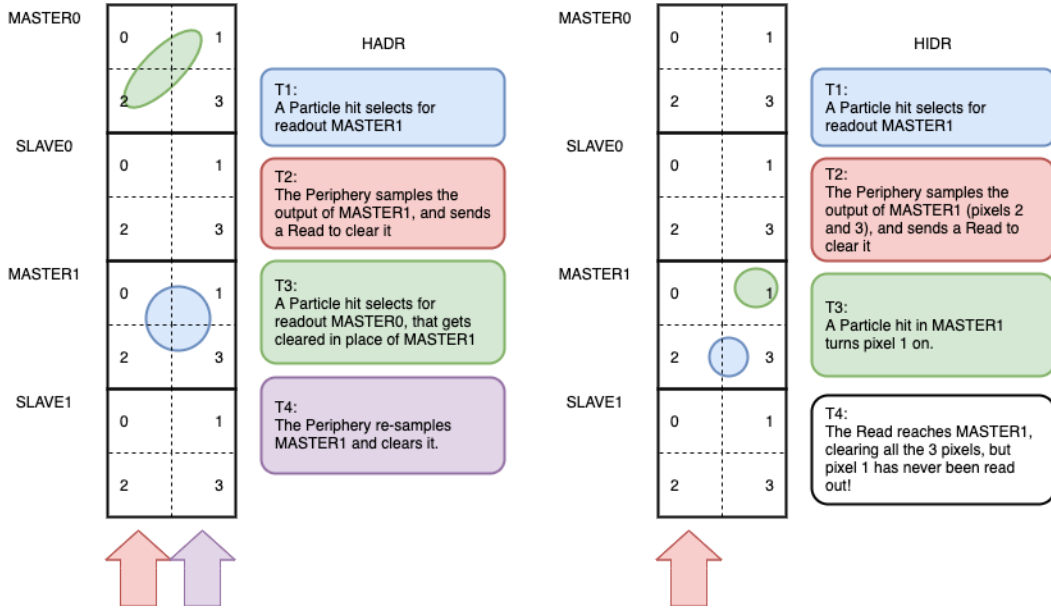


Figure 5.4

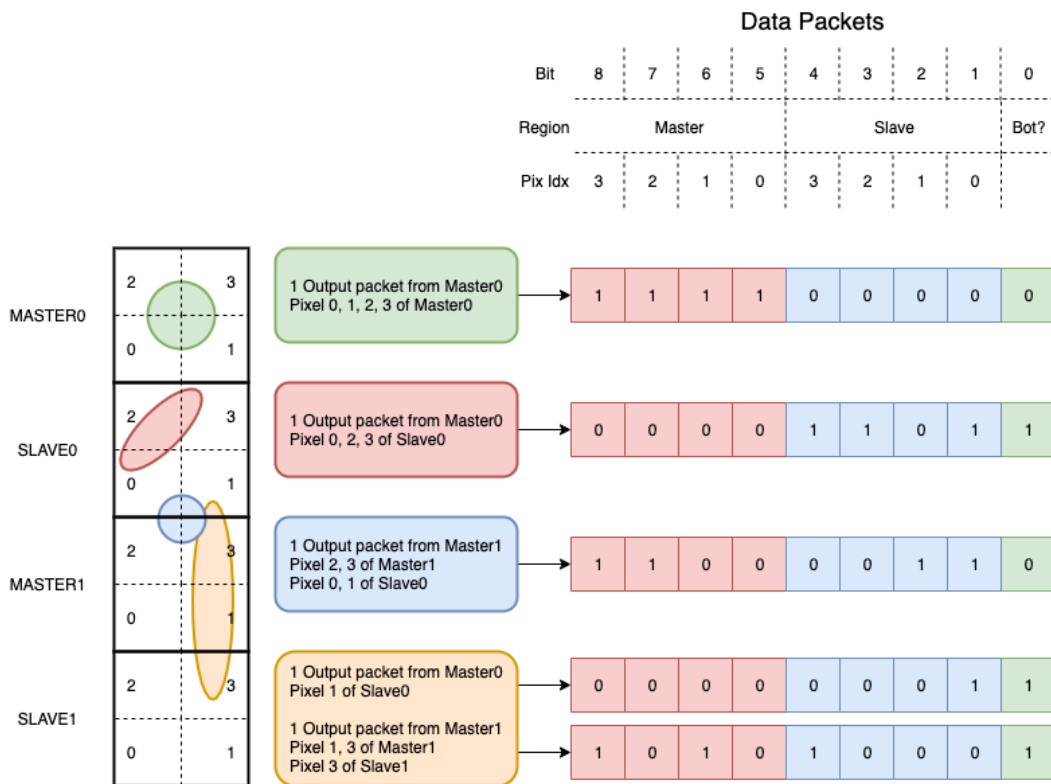


Figure 5.5

ment complex functionality in the pixel matrix, sharing resources among many pixels as needed.”. pagina 28 della review.

888

889 TABELLA: con la gerarchia del chip Matrix (512x512 pixels) Section (512x32 pixels)
890 Column (512x2) Core (32x2) Region (4x2)

891 Nel chip trovi diverse padframe: cosa c’è nelle padframe e End of section.

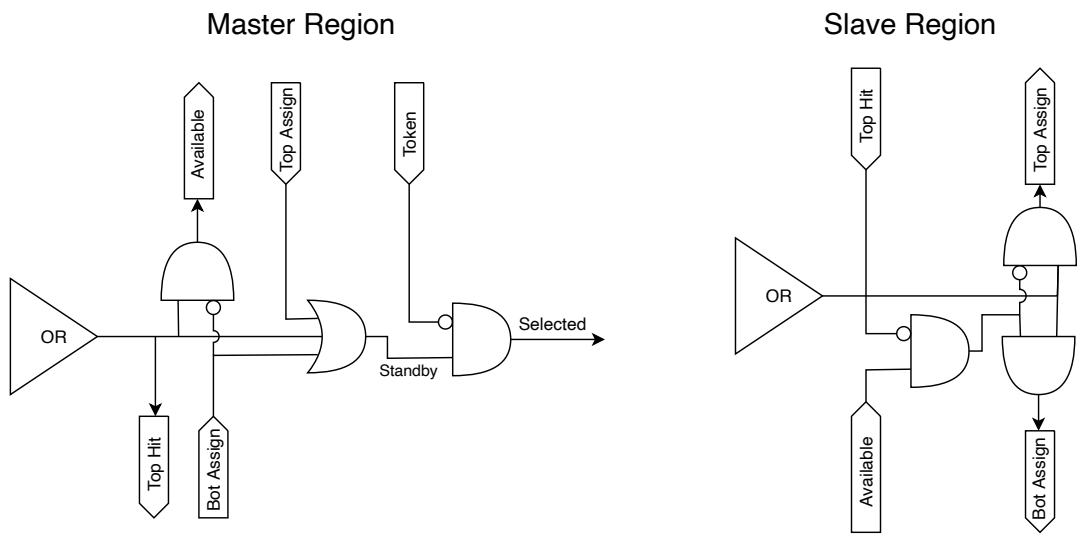


Figure 5.6

892 "DC-balance avoids low frequencies by guaranteeing at least one transition every n
 893 bits; for example 8b10b encoding n =5"

894 **Chapter 6**

895 **Characterization**

896 **6.1 TJ-Monopix1 characterization**

897 **6.1.1 Threshold and noise: figure of merit for pixel detectors**

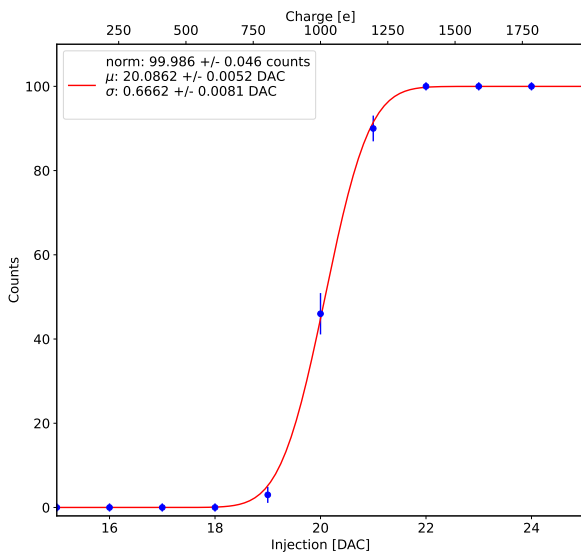


Figure 6.1: S-curve for pixel (10, 10) of the PMOS flavor (flavor 1) with IDB fixed at 40 DAC. The conversion of charge injected from DAC to electrons has been done assuming a conversion factor of 20 e⁻/DAC.

898 A characterization of threshold and noise is typically necessary since these values have
899 an impact on the operating conditions and on the performance of the chips. infact, the
900 signal to threshold ratio may be considered as the figure of merit for pixel detectors rather
901 than the signal to noise ratio. The mean minimum stable threshold evolved through
902 different generation of chips: in the 1st generation it was around 2500 e⁻ while in the
903 3rd (corresponding to nowadays chips) is less than 500 e⁻. This allows in thinner sensors
904 with smaller signals: from 16 000 e⁻ produced in 200 μ m, the signal expected moved down
905 to 2000 e⁻ produced in 25 μ m. According with this ??, the threshold of TJ-Monopix1 is
906 around 500 e⁻. The following prototypes have lower threshold and noise, for example TJ-
907 Monopix2 has **check**, according to the above. The threshold has to be located between the

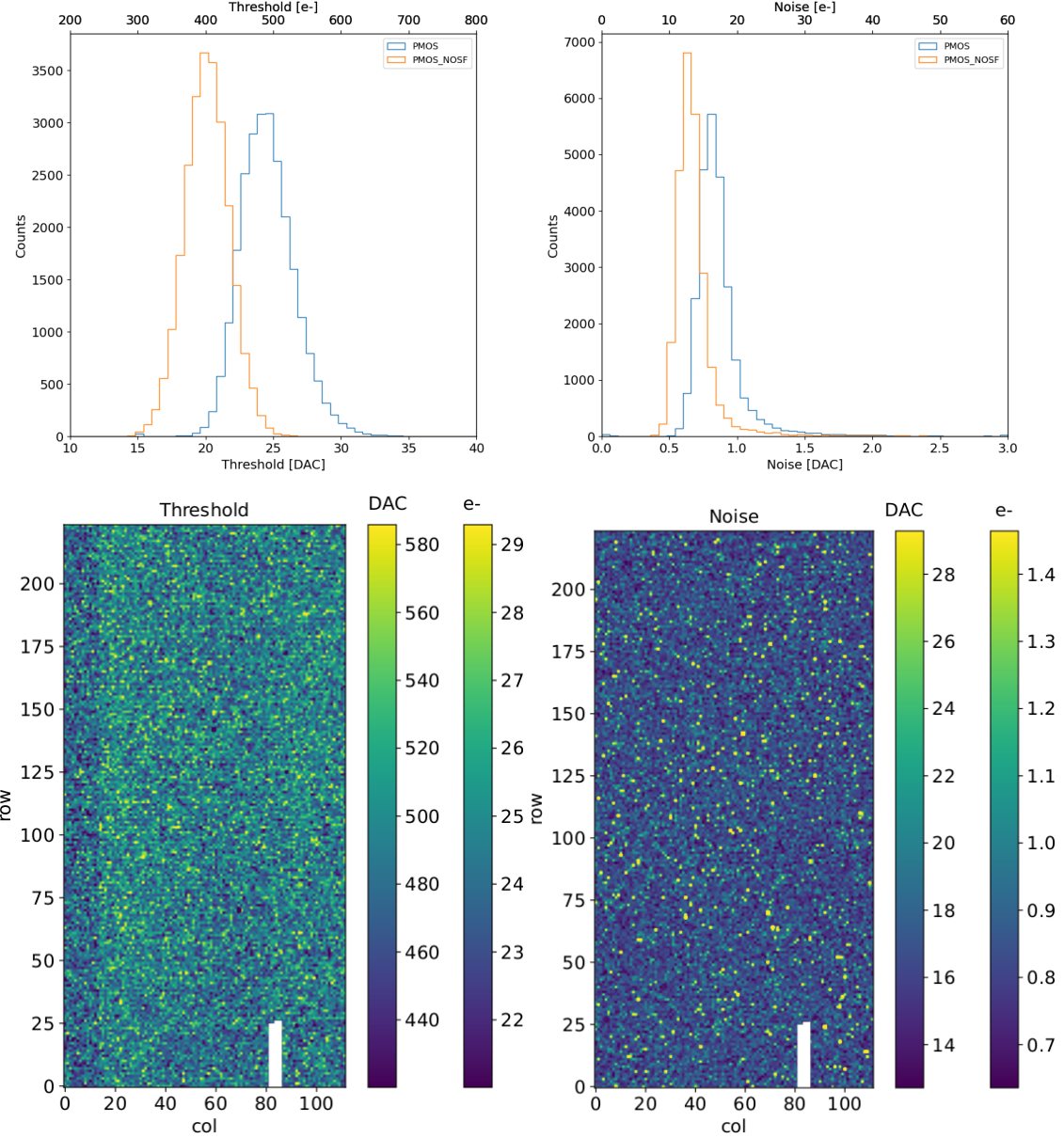


Figure 6.2: Histograms of the threshold (a) and the noise (b) found fitting the s-curve of all flavor with IDB fixed at 40 DAC. Maps of the threshold (a) and the noise (b) found fitting the s-curve with IDB fixed at 40 DAC. The white pixels have the injection circuit broken.

noise peak around the baseline and the signal distribution, in particular it has to be low enough to maintain a high signal efficiency, but also high enough to cut the noise: for a low threshold many pixels can fire at the same time and a positive feedback can set off a chain reaction eventually, causing all the other pixels to fire. Thus, the noise sets a lower bound to the threshold: if an occupancy $\leqslant 10^{-4}$ is required, for example, this corresponds to the Gaussian 1-sided tail fraction for 3.7σ . In this case, if the noise is 100 e- , for example, the threshold must be higher than $3.7 \times 100\text{ e-}$. Typically this argument sets only a minimal bound to the threshold since the variation with time and from pixel to pixel have to be taken into account: the temperature, the annealing (for example, the radiation damages in the oxide layer causes shift of MOSFET threshold voltage) and the process parameters

918 variation across the wafer (as for example process mismatch between transistors).

919 On the other hand the noise is valued at the preamplifier input node given that the
920 first stage of amplification is the most crucial since the signal amplitude is high compared
921 to additional noise introduced by the following stages. The noise is then parameterized as
922 Equivalent Noise Charge (ENC), which is defined as the ratio between the noise N at the
923 output expressed in Volt and the out voltage signal S produced by 1 e⁻ entering in the
924 preamplifier:

$$ENC = \frac{N_{out}[V]}{S_{out}[V/e^-]} = \frac{V_{noise}^{RMS}}{G} \quad (6.1)$$

925 with G expressed in V/e⁻; as the gain increases, the noise reduces .

926 **ENC is mainly influenced by the total input capacitance and by the system band-**
927 **width: if the bandwidth is constant, noise can be reduced by increasing the input transis-**
928 **tor transconductance (and consequently power consumption).** Considering the threshold
929 dispersion a requirement for the ENC is:

$$ENC < \sqrt{(T/3.7)^2 - T_{RMS}^2(x) - T_{RMS}^2(t)} \quad (6.2)$$

930 where the T is the threshold set, T_{RMS} is the threshold variation during time (t) and
931 across the matrix (x); a typical reasonable value often chosen is 5 ENC.

932 Because of the changing of the 'real' threshold, the possibility of changing and adapting
933 the setting parameters of the FE, both in time and in space is desiderable: these parameters
934 are usually set by Digital to Analog Converter (DAC) with a number of bit in a typical
935 range of 3-7. Unfortunately DAC elements require a lot of space that may be not enough
936 on the pixel area; therefore, the FE parameters are typically global, which means that they
937 are assigned for the whole chip, or they can be assigned for regions the matrix is divided
938 into. The former case corresponds to TJ-Monopix1's design in which 7 bits are used for
939 a total 127-DAC possible values, while the latter corresponds to the ARCADIA-MD1's
940 one, **where quanti bit??**. An other possibility, for example implemented in TJ-Monopix2,
941 is allocate the space on each pixel for a subset of bits, then combinig the global threshold
942 with a fine tuning. If so, the threshold dispersion after tuning is expected to be inversely
943 proportional to the tuning DAC number of bits and thus be improved a lot:

$$\sigma_{THR,tuned} = \frac{\sigma_{THR}}{2^{nbit}} \quad (6.3)$$

944 where σ_{thr} is the RMS of the threshold spread before tuning.

945 To measure the threshold and noise of pixels a possible way is to make a scan with
946 different known injected charge: the threshold corresponds to the value where the efficiency
947 of the signal exceeds the 50%, and the ENC is determined from the width of this edge.
948 Following this path, I have used the injection circuit available on the chip to inject 100
949 pulses for each input charge for a fixed threshold. The injection comes on a capacity at the
950 input of the FE circuit, whose mean value is 230 aF and from which the conversion factor
951 from DAC units to electrons can be obtained: for the PMOS flavor, for example, since
952 the DAC are biased at 1.8 V, the Least significant Bit (LSB) corresponds to a voltage of
953 14.7 mV from which the charge for LSB 1.43 e⁻/mV and the conversion factor therefore
954 is 20.3 e⁻/DAC. While this value is equivalent for all the PMOS flavor, the HV flavor
955 is expected to have a different conversion factor, ~ 33 e⁻/DAC, beacuse of the different
956 input capacity.

957 Besides the charge, also the duration and the period of the injection pulse can be set;
958 it is important to make the duration short enough to have the falling edge during thed

	DAC units	electrons
Threshold	24.529 ± 0.049 u: 24.433 ± 0.049 d: 24.623 ± 0.051	
Threshold dispersion	1.848 ± 0.033 u: 1.867 ± 0.034 d: 1.825 ± 0.035	
Noise	0.8222 ± 0.0043 u: 0.8225 ± 0.0045 d: 0.8221 ± 0.0043	
Noise dispersion	0.0975 ± 0.0030 u: 0.0968 ± 0.0031 d: 0.0970 ± 0.0030	

Table 6.1: Flavor PMOS, IDB fixed at 40 DAC

dead time of the pixel (in particular during the FREEZE signal) in order to avoid the undershoot, coming at high input charge, triggering the readout and reading spurious hits. Since the injection circuit is coupled in AC to the FE, if the falling edge of the pulse is sharp enough to produce ad undershoot, this can be seen as a signal.

Assuming a gaussian noise, the efficiency of detecting the signal can be described through a modification of the error function:

$$f(x, \mu, \sigma) = \frac{1}{2} \left(1 + \operatorname{erf} \left(\frac{x - \mu}{\sigma\sqrt{2}} \right) \right) \quad (6.4)$$

with: where the threshold and the ENC corresponds to the μ and σ . Therefore I perform a fit of the counts detected using the function in equation 6.4. In figure 6.1 there is an example with IDB (look at table 6.1 for the meaning of the parameter) equal to 40 DAC of fit for a pixel belonging to the flavor 1, while in table 6.1 and figure ?? and ?? there are the histograms and the maps of the parameters of the scurve-fit.

To verified the trend of the threshold as a function of the front end parameter IDB, I have permormed a scan with different IDBs: I have injected the whole matrix and found the means and the standard deviation of the distributions. The results are shown in figure 6.3.

6.1.2 Linearity of the ToT

I have already said in chapter ?? that TJ-Monopix1 returns an output signal proportional to the charge released by a particle in the epitaxial layer, which is the Time over Threshold; the ToT is saved as a 6-bit variable and then has a dynamic range equal to 0-64, which corresponds to 0 μ s to 1.6 μ s assuming a clock frequency of 40 MHz. When a pulse is longer than 1.6 μ s the counter rolls back to zero and there is no way to distinguish that charge from a lower one with the same ToT: that is the rollover of the ToT (??(a)).

In order to associate the ToT (in range 0-64) to the charge, a calibration of the signal is necessary. Assuming the linearity between ToT and the charge, Q can be found:

$$Q [\text{DAC}] = \frac{(ToT [\text{au}] - q [\text{au}])}{m [\text{au}/\text{DAC}]} \quad (6.5)$$

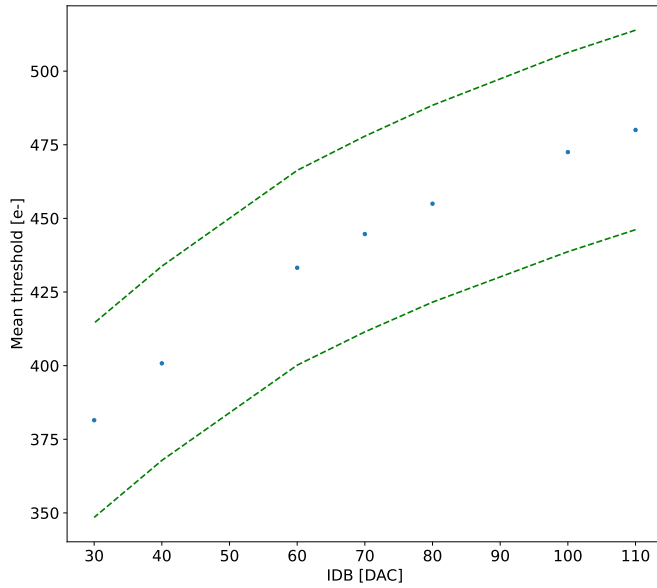


Figure 6.3

983 where m and q are the fitted parameters of the calibration. It is important to keep in
 984 mind that the main application target of TJ-Monopix1 is in the inner tracker detector of
 985 HEP experiments, then the main feature is the efficiency, then a rough calibration of the
 986 signal to charge is fine; **this information can be used to improve??.**

987 The study of the output signal is made possible via the injection: since the pulses
 988 are triangular, the ToT is expected to be almost linear depending on the injection charge
 989 value. To verify this statement and study the deviations from linearity I've fit the ToT
 990 versus the charge injected for all pixel within the matrix. In figure ??(b) there is an
 991 example of fit for a pixel belonging to the flavor 1, while in figure 6.5 and ?? there are the
 992 histograms and the maps of the parameters of the line-fit for all flavors with IDB fixed at
 993 40 DAC.

994 Before performing the fit I have calculated the mean value of the ToT of the pulses
 995 recorded for each pulse amplitude and I used the mean ToT as value for the fit. The aim
 996 of the calibration obviously is finding a relation only in the range 0-64 without taking into
 997 account the rolling over hits: therefore, to prevent the rollover data from reducing the
 998 mean ToT introducing a bias in the mean value, I cut and I did not consider them. If a
 999 signal bigger than the $1.6 \mu\text{s}$ is expected in the usage of the detector, the threshold must be
 1000 raised or the gain reduced, making the expected output signal in range 0-64. In figure ??
 1001 (b) are shown both the fits with a line (red) and with a second order polynomial (green):
 1002 at the bounds of the ToT range values deviate from the line model. Since the deviation is
 1003 low than **controlla quant'era, questo ha un impatto sul valore della calibrazione di tipo ..**
 1004 **che è trascurabile al primo ordine. e comunque hai problemi ai bounds mentre al centro**
 1005 **hai comunque una buona linearità.. Chiarire la differenze negli istogrammi e come mai ci**
 1006 **sono delle bande nelle mappe.**

1007 perché noise e th sono diverse per diversi flavor? Controlla cos' hanno di diverso.

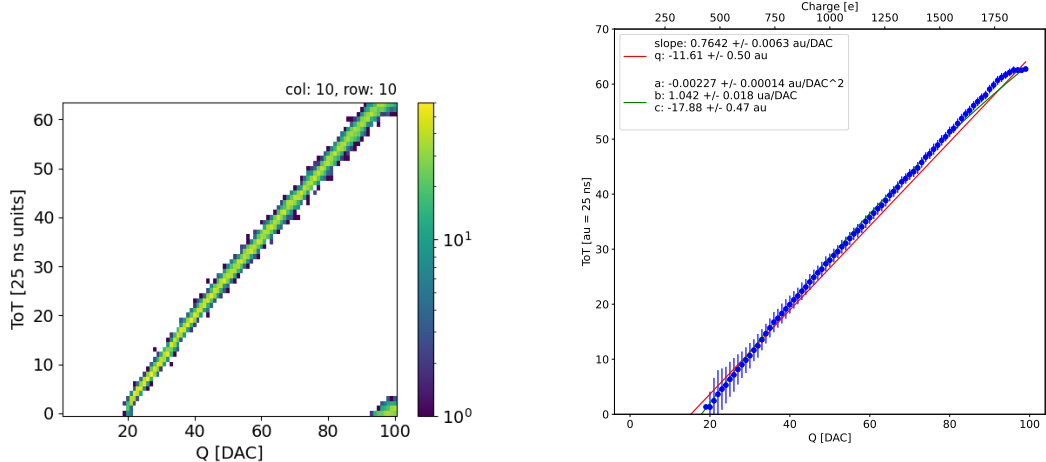


Figure 6.4: The figures refer to pixel (10,10) of the PMOS-reset flavor (1) with IDB fixed at 40 DAC. (a) Histogram of the injection pulses: the ToT is in range 0-64 since it is represented by 6 bit, so when achieving the 64 it rolls over back to the zero. (b) Mean ToT vs the the charge: the mean has been calculated cutted the rolling hits.

	PMOS 0	PMOS 1	PMOS 2	HV
Slope [au/DAC]	0.75566 ± 0.00149	0.57145 ± 0.00025		
Slope dispersion [au/DAC]	0.03841 ± 0.00037	0.01685 ± 0.00016		
Intercept [au]	-11.6070 ± 0.0089	-10.824 ± 0.019		
Intercept dispersion [au]	1.5176 ± 0.0063	1.225 ± 0.013		

Table 6.2: Mean calibration parameters for all flavor and their dispersion on the matrix.

1008 6.1.3 Calibration of the ToT

1009 Considering that the charge injected in the FE goes to fill capacitor which is different from
 1010 pixel to pixel, the true charge injected does not correspond to what expected assuming C
 1011 equal to 230 aF, the nominal value. Accordingly to that, a verification of the value provided
 1012 and an absolute calibration of this capacity and of the conversion factor F is needed to
 1013 have a correspondence of the signal in electrons; assuming C 230 aF, F is expected to be
 1014 $20 e^-/\text{DAC}$, and is defined as:

$$F [e^-/\text{DAC}] = \frac{1616 e^-}{Q [\text{DAC}]} \quad (6.6)$$

1015 For this purpose a Fe55 radioactive source has been employed; the Fe55 is an extremely
 1016 important radionuclide in the calibration of X-ray spectrometers, proportional counter
 1017 and scintillator detector since it emits two X-photons during the electron capture
 1018 decay: the first one (K_α) at 5.9 keV and the second one (K_β) at 6.5 keV. The K_α photon,
 1019 which does photoelectric effect in the silicon, has an absorption length $\lambda = 7 \mu\text{m}$ to $8 \mu\text{m}$,
 1020 and the probability of being absorbed in the $25 \mu\text{m}$ thick epitaxial layer is ~ 0.95 . The
 1021 electron emitted has an energy equal to the photon one, so recalling that the mean energy
 1022 needed to produce a couple electron-vacuum is 3.65 eV, the signal produced by the Fe55
 1023 source is expected to be $1616 e^-$. In figures ?? and ?? are shown two histograms of the
 1024 ToT spectrum of the Fe55 source for two different pixels. The peak corresponds to the

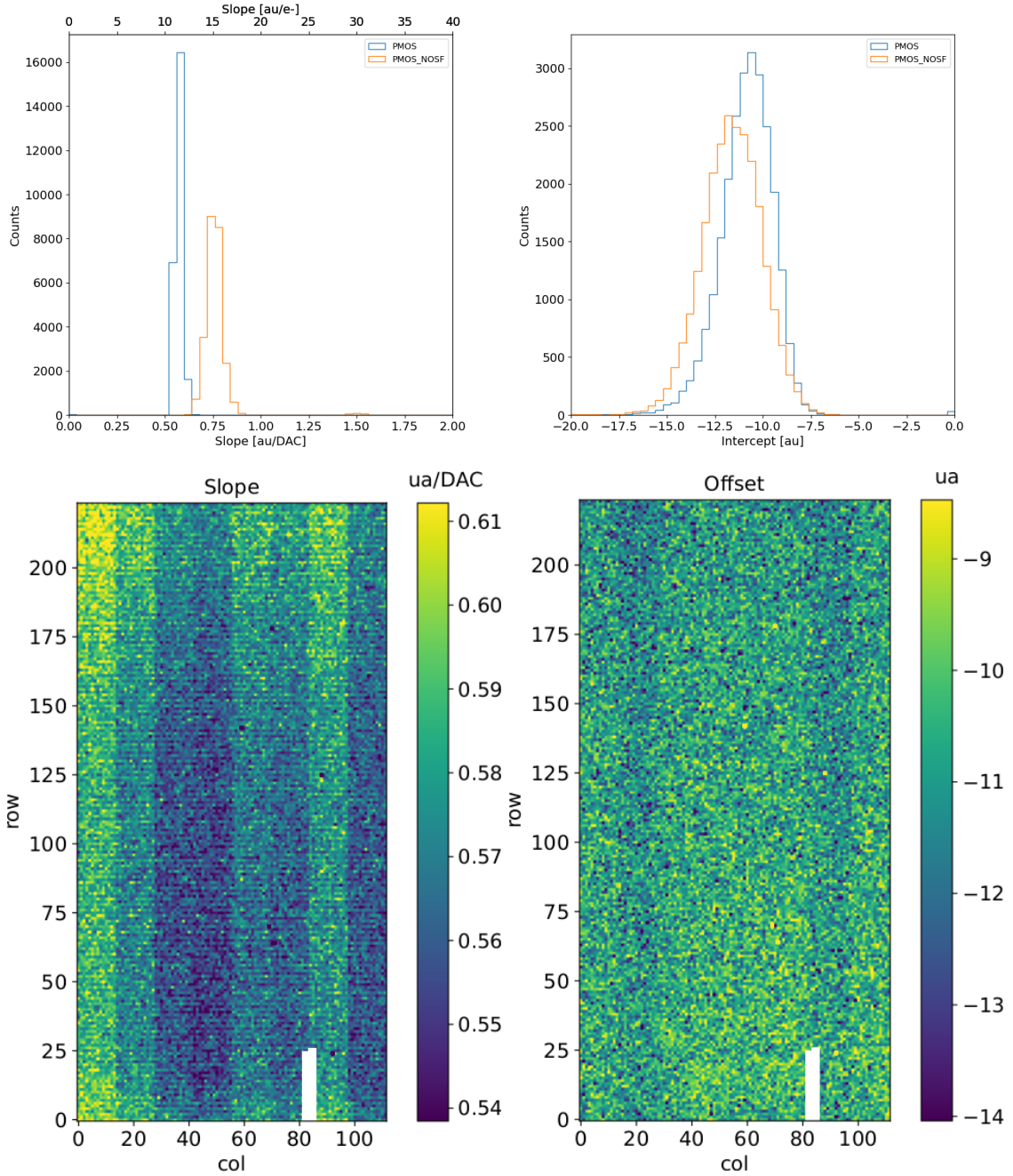


Figure 6.5: Histograms of the calibration parameters, slope (a) and offset (b), found fitting the ToT with a line, for all flavor and with IDB fixed at 40 DAC. Maps of the calibration parameters, slope (a) and offset (b), found fitting the ToT with a line, with IDB fixed at 40 DAC

events with completely absorption of the charge produced in the depleted region, while the long tail on the left to all the events with partial absorption due to charge sharing among neighbors pixels. In order to reduce the charge sharing, the pixel dimension in TJ-Monopix2 has been reduced down to [check](#). The events on the right side of the peak, instead, corresponds to the K_β photons. Looking at the histograms for pixel (30, 185) and (30, 69) a significant difference in the peak to tail ratio leaps out. This difference in the efficiency of detecting the signal can be related with the position of the pixel in the matrix:

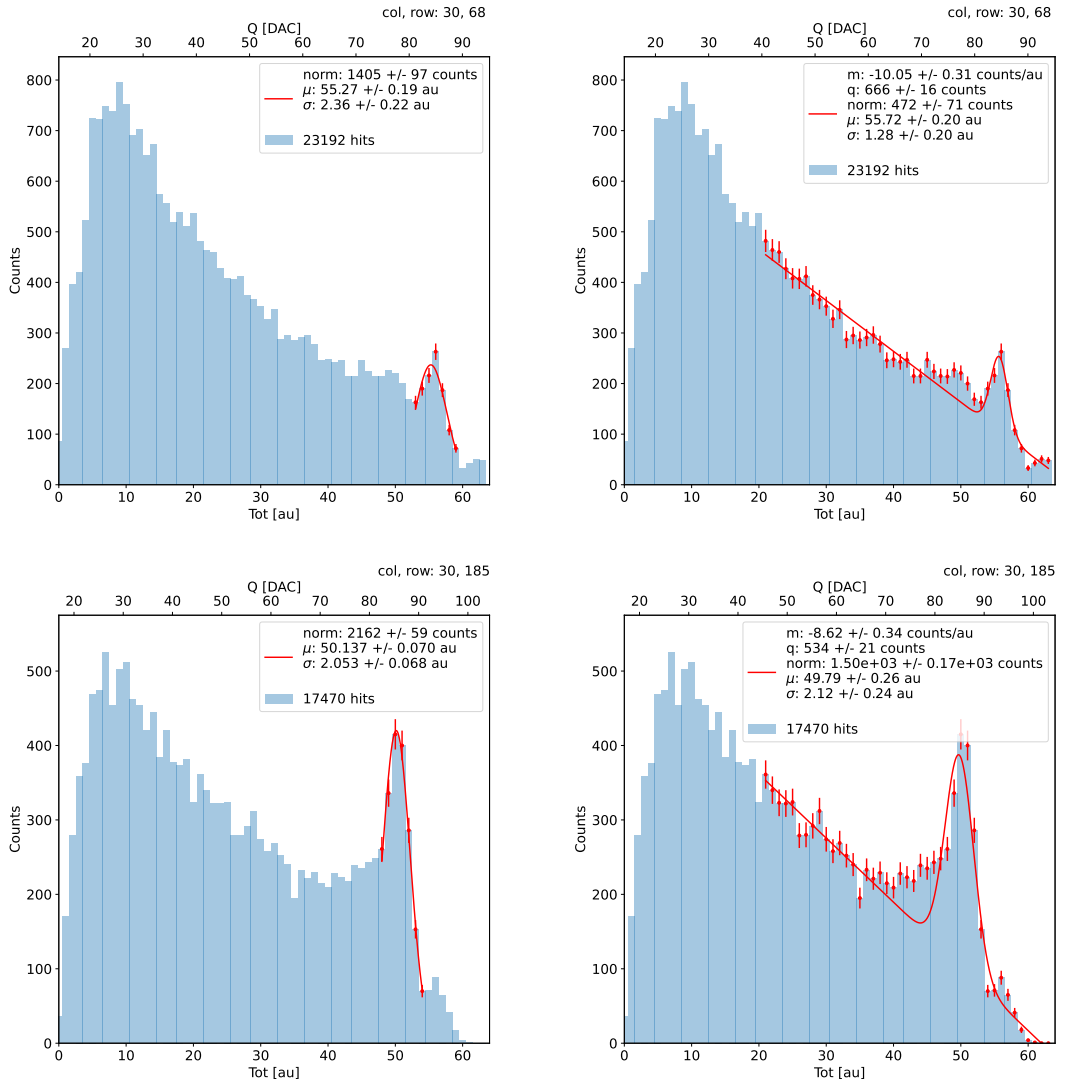


Figure 6.6: due pixel per far vedere la differenza tra i fit. Sottolinea che in rosso ci sono i bin fittati. La doppia scala utilizza le info trovate nel paragrafo precedente per il dato pixel in questione. Per avere una corrispondenza grezza in elettroni basta moltiplicare per 20 e- / dac.

in particular pixels in the upper part of the matrix (rows 112-224) have a more prominent peak, while in pixels in the lower part (rows 0-111) there is a higher partial absorption. I recall now that there is a slightly difference in the structure of the low dose-epi layer (???) among the rows in the matrix, in particular pixels in rows 112-224 are supposed to have a higher efficiency in the pixel corner.

For the calibration I have need to establish the peak position; to do that I perform a fit of the ToT histogram of each pixels. As fit functions I test both the solutions below:

$$f(x, N, \mu, \sigma) = \frac{N}{\sigma\sqrt{2\pi}} e^{-\frac{1}{2}(\frac{(x-\mu)}{\sigma})^2} \quad (6.7)$$

$$f(x, m, q, N, \mu, \sigma) = m x + q + \frac{N}{\sigma\sqrt{2\pi}} e^{-\frac{1}{2}(\frac{(x-\mu)}{\sigma})^2} \quad (6.8)$$

Nel primo caso ho fissato pochi pixel attorno a picco: il range è stato determinato ..

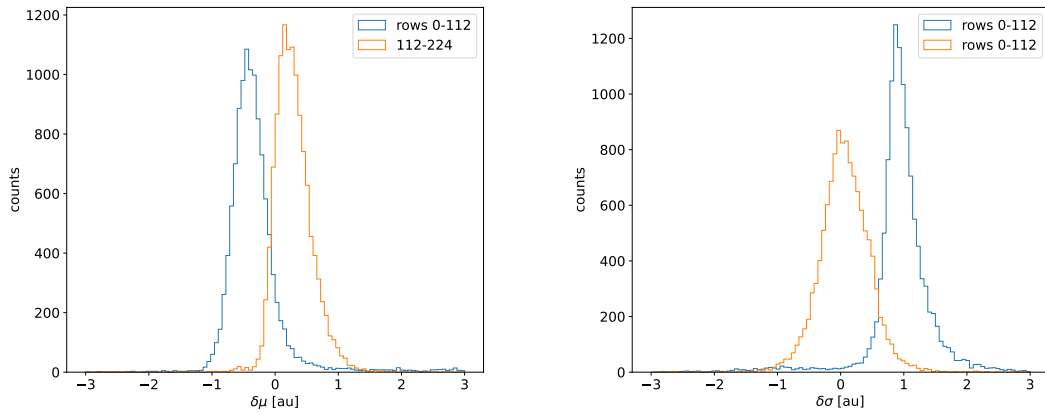


Figure 6.7: Here there are shown the defference between the parameters μ and σ fitted with only a gaussian and with a gaussia plus a line. When $\mu < 0$ the fit function 6.7 has given a worst peak (shifted on the left); when $\sigma < 0$, 6.8 has given a worst peak width (larger sigma)

1040 controlla. Nel secondo caso invece il range è.. Controlla sullo script Even if the difference
 1041 in the peak position between the two cases is not really relevant (6.7) being of the order
 1042 of 0.8-1.5 %, it still introduces a systematic effect moving the peak on the left because of
 1043 the contribution of the tail. Indeed, we know that the sharp edge on the right corresponds
 1044 to the complete absorption of the photon, so excluding the little bump on the right, the
 1045 more the fitted parameter is on the right, the better the fit is. Moreover, there is also
 1046 systematic effect on the peak width, infact the worst fit also gives an overestimation of
 1047 the peak width. Even looking at the χ^2 , the fit function 6.7 seems so be the better choise,
 1048 except for a sample of pixels on the lower part of the matrix, the one with lower efficiency.

1049 Mappa del ferro da cui, come descritto enll'equazione si ricava la capacity. La struttura
 1050 a bande della capacità ha origine nel plot... e quindi nella calibrazione. Andando a vedere
 1051 gli istogrammi di queste due variabili si vedono dei picchi. C'è qualche struttura nella
 1052 matrice che condiziona il funzionamento delle righe? Larghezza della gaussiana: fai il
 1053 discorso a cosa contribuisce ad un picco così largo. è compatibile con quanto ti aspetti?

1054 6.1.4 PMOS flavor: changing the bias

1055 In order to study the behavior of the sensor changing the bias, I perform some injection
 1056 scans in different configurations. The thickness of the depletion has to be considered
 1057 indeed an important parameters for the efficiency of the signal, and in particular it plays
 1058 an important role if bho, trova qualcosa da dire.

1059 Given that the chip under examination has a gap in the low dose epi-layer (look at
 1060 chapter ??) we were not able to change independently the bias of the substrate (PSUB)
 1061 and of the p-well (PWELL), but they must be kept at the same value, differently from
 1062 other chips, where thay can be changed as reported in figure 4.10. Turning down the bias,
 1063 the depletion region narrows and the efficiency reduces in particular in the pixel corner; La
 1064 soglia si alza di meno di 1/3, mi sarei aspettata un po' di più guardando il plot. Attenzione
 1065 che il plot non è fatto con un ngap, quindi ci sta che il guadagno lì cali più bruscamente.
 1066 poi non si capisce benissimo dalla colormap. Anche la slope diminuisce di circa meno di

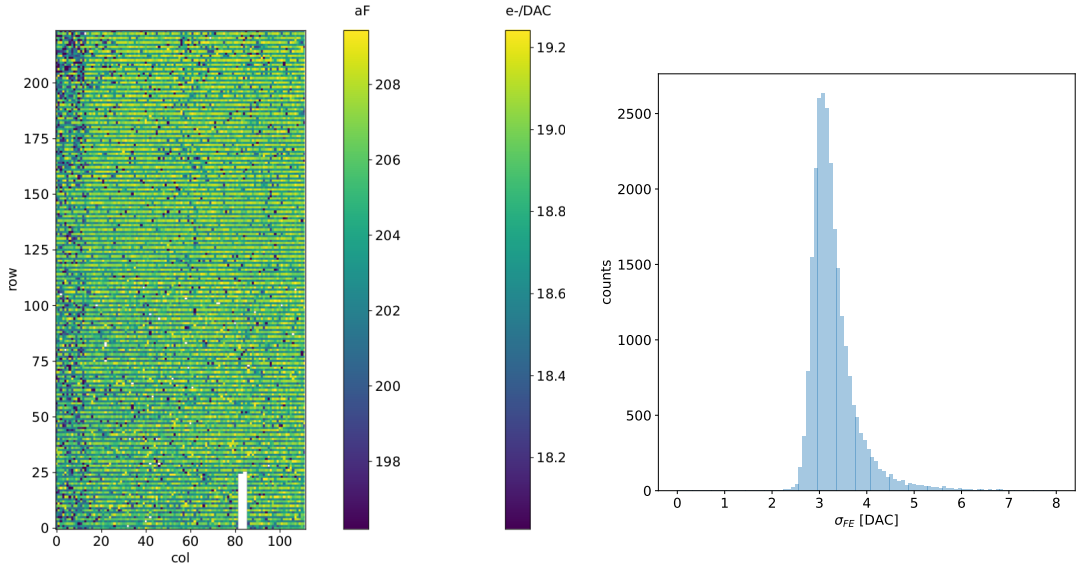


Figure 6.8

	-6 V	-3 V	0 V
Threshold [DAC]	20.04 ± 1.6	21.0 ± 1.6	24.5 ± 1.8
Noise [DAC]	0.613 ± 0.075	0.625 ± 0.078	0.822 ± 0.098
Slope [au/DAC]	0.726 ± 0.027	0.707 ± 0.028	0.573 ± 0.021
Offset [au]	-10.8 ± 1.9	-11.2 ± 1.8	-11.1 ± 1.5

Table 6.3: The errors are the standard deviations of the corresponding distributions.

1067 un terzo. Il noise aumenta leggermente. Il picco del ferro invece si sposta a sinistra di
 1068 un terzo. Lo spostamento è dovuto alla diminuzione del gain, che influisce sul ToT.

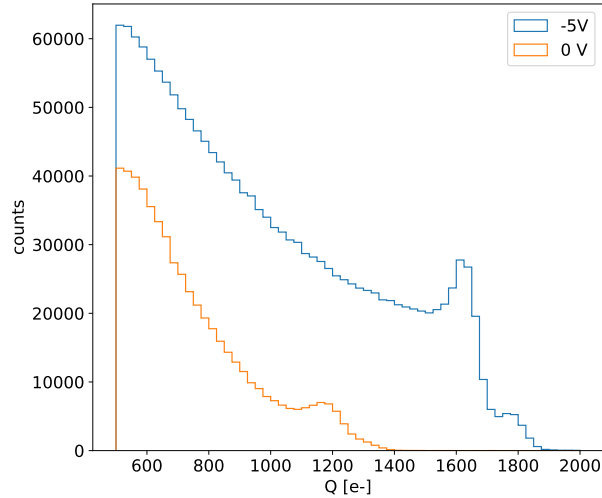


Figure 6.9: With the same acquisition time.

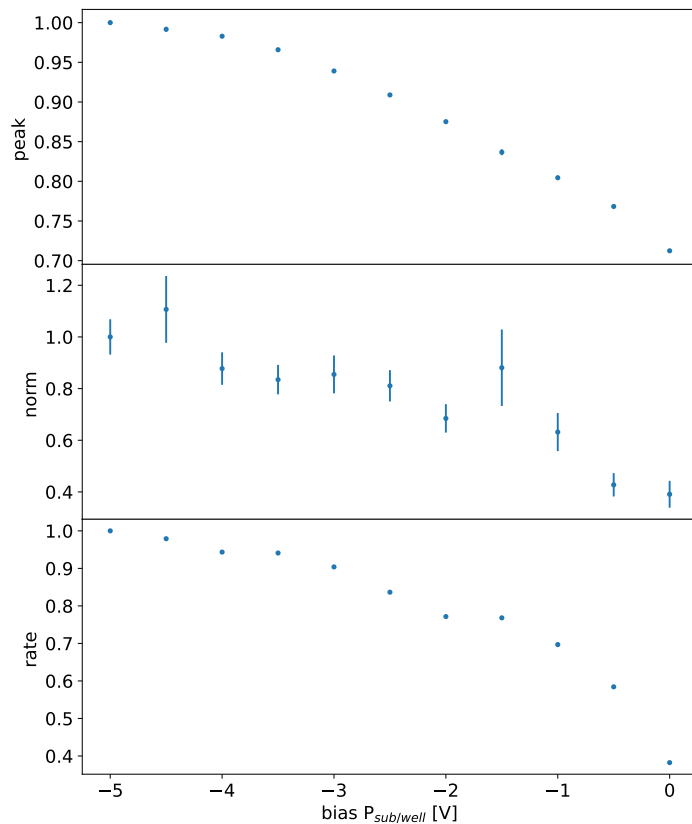


Figure 6.10: da rifare tenendo la sorgente ferma tra un’acquisizione e l’altra

1069 6.1.5 Measurements with radioactive sources

1070 Signal response characterization using radioactive sources and cosmic rays have been made.

1071 The Sr90 source emits electrons that: lo spettro ha un cutoff a che E?

1072 **conto/plot sulla differenza elettrone sr e mip.** The signal generated by electrons is sim-
1073 ilar to the one generated by minimum ionizing particle (MIPS). The spectrum is expected
1074 to follow a Langau-Gauss distribution

- 1075 • sommato i cluster Spiega la tua definizione di cluster.
- 1076 • plot dello spettro del ferro convertendo in elettroni per il PMOS flavor e facendo la
1077 somma dei cluster.
- 1078 • di che la tua definizione di cluster è ok perchè sono quasi tutti vicini: plot con la
1079 distanza e qualche stima delle coincidenze casuali.
- 1080 • mappa di qualche evento di cluster sia per Sr che per FE
- 1081 • istogrammi in carica, con carica sommata di Sr e Fe, oer il flavor PMOS dove hai
1082 fatto la calibrazione o per tutti?

1083 Spiega che con il flavor HV abbiamo una perdita di segnale, fai vedere uno spettro di
1084 delle misure dell’8 marzo.

1085 6.1.6 Dead time measurements

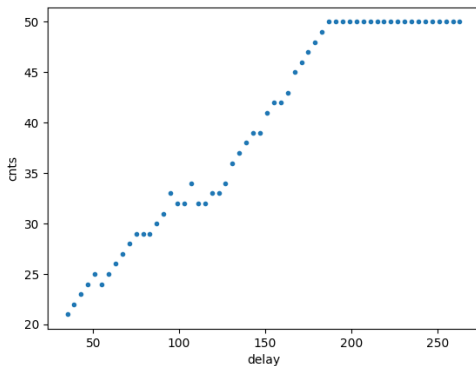
1086 The hit loss is due to analog and digital pile up: the first one occurs when a new hit
 1087 arrives during the pre-amplifier response, the second instead, which is the more relevant
 1088 contribution with high rate, while the information of the previous hit has not yet been
 1089 transferred to the periphery. As only one hit at a time can be stored on the pixel's RAM,
 1090 until the data have completed the path to get out, the pixel is paralyzed and the dead time
 1091 τ almost corresponds with the time needed to trasmit the data-packets off-chip. Since the
 1092 exportation of data from pixel to the EoC occurs via a 21-bits data bus, only one clock
 1093 cycle is need to transfer the data to the end of column and the dead time bottleneck is
 1094 given by the bandwidth of the serializer at the EoC. In our setup the serializer operates
 1095 at 40 MHz, thus to transmit a data packet (27-bit considering the addition at the EoC)
 1096 at least 675 ns are needed. For what we have said so far, the R/O is completely sequential
 1097 and therefore is expected a linear dependence of the reading time on the number of pixels
 1098 to read:

$$\tau = 25 \text{ ns} \times (\alpha N + \beta) \quad (6.9)$$

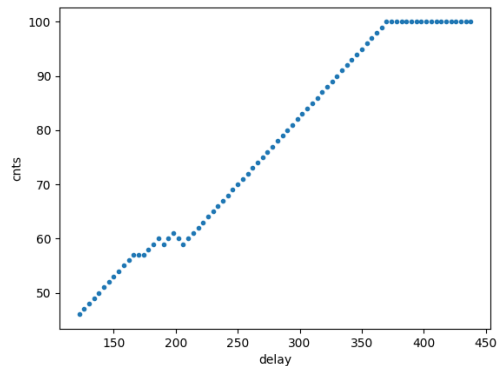
1099 where α and β are parameters dependent on the readout chain setting.

1100 To measure and test the linearity of the reading time with the number of pixels firing,
 1101 I have used the injection mode available on the chip. Indeed, the injection mode allows
 1102 fixing not only the amplitude of the pulse, which corresponds to the charge in DAC units,
 1103 but also the period and the width. I have injected a fix number of pulses (100) and looked
 1104 for the rate when the efficiency decreases. Moreover to test that there is no dependece of
 1105 the digital readout time from the charge of the pulse, I have try to change the amplitude of
 1106 the pulse injected, but the parameters found were consistent with the default configuration
 1107 ones.

1108 Al posto degli esempi con 5 e 10 pixels metterei un esempio dell'efficienza vs il periodo
 1109 quando leggo un singolo pixel. Una cosa che volevo fare era anche provare a fittare la slope
 1110 con cui l'efficienza scende: se la slope è uguale per tutti il readout diventa completamente
 predittivo.



(a) efficiency vs DELAY 5 pixels



(b) efficiency vs DELAY per 10pixels

1111 While the single pixel reading time and the dead time do not depend on the position
 1112 on the pixel matrix and are equal to 106 (46+60) clock counts within 1 clock count, on
 1113 the other hand the τ depends on the pixel position on the matrix when more than one
 1114 pixel are firing. In particular the priority chain goes from row 224 to row 0, and from col
 1115

Parameter	Value [DAC]	Value [μ s]
START_FREEZE	64	1.6
STOP_FREEZE	100	2.5
START_READ	66	1.65
STOP_READ	68	1.7

Table 6.4: Default configuration of the R/O parameters

1116 0 to 112, that means the last pixels to be read is the one on le bottom right corner of the
 1117 matrix.

1118 In figure 6.13 is reported the reading time versus the number of pixels injected; the
 1119 R/O parameters that control the reading time and their default values are reported on
 1120 table ??.

1121 The factor α , referring to eq. 6.9 is proportional to the difference (STOP_FREEZE
 1122 - START_READ), while the offset β lies between 5 and 15 clock counts. Since through
 1123 the injection a random hit rate on the matrix can't be simulated, as the coordinates
 1124 of the pixels to inject must be specified, for convenience I used the pixels on the same
 1125 column/row. No difference in the α and β coefficients has been observed between the two
 case.

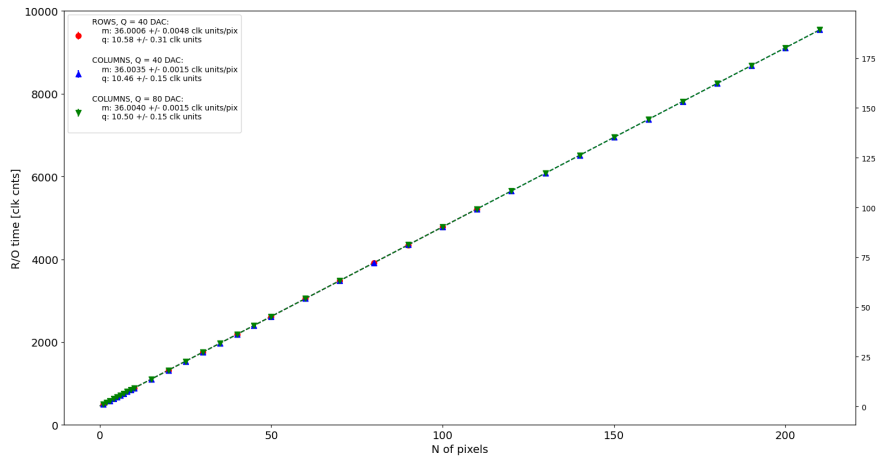


Figure 6.12

1126
 1127 Ci sarebbe da spiegare perchè i parametri che usiamo noi come default non sono quelli
 1128 che minimizzano il tempo di lettura. La spiegazione è che "Abbiamo copiato i valori
 1129 dal repository di quelli di Bonn". Un'altra domanda potrebbe essere: come mai non ho
 1130 esplorato una zona più vasta per i parametri del R/O. Cambiando molto i parametri del
 1131 R/O la lettura non funzionava per niente: ad esempio CONF_STOP_FREEZE non può
 1132 essere impostato nè sopra 105 nè sotto 95

1133 6.2 ARCADIA-MD1 characterization

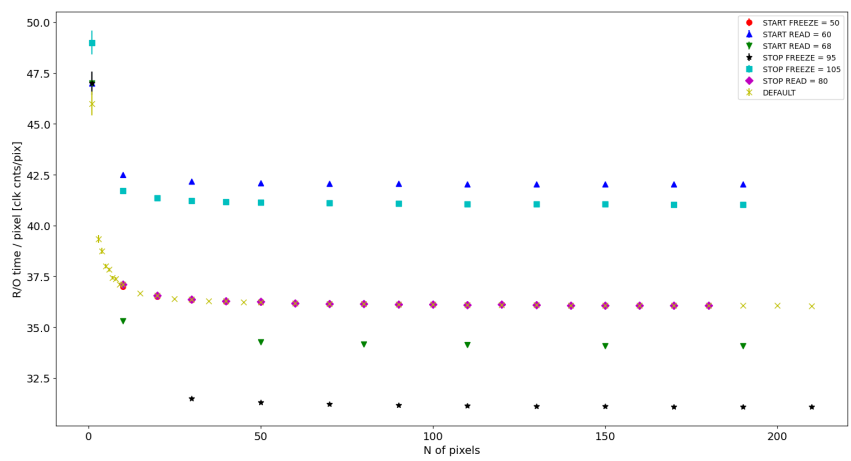


Figure 6.13

1134 **Chapter 7**

1135 **Test beam measurements**

1136 During August 2022 a testbeam took place in Santa Chiara hospital in Pisa, where a
1137 new accelerator designed for both medical research and R&D in FLASH-RT, and for this
1138 reason called "ElectronFlash", have been installed a few months ago.

1139 The motivation of the testbeam measurements were testing TJ-Mopopix1 in condition
1140 different from the one foreseen during the design and also testing the mechanical and the
1141 DAQ setup for other future measurement. TJ-Monopix1 is supposed to be employed for
1142 tracking in HEP experiments while our goal was testing the possibility of integrating the
1143 charge released by more particles at ultra high hit rate achievable with the accelerator.

1144 **Una frase di disclaimer sul fatto che non siamo riusciti a testare quello che volevamo.**

1145 In medical physics the dose is indeed the standard parameter to characterize the beam
1146 because of its obvious relation with the damage caused in the patient: firstly the oncolo-
1147 gists prescribe a certain dose taking into account the efficacy of the treatment and then
1148 the medical physicists, on the basis of simulations, decide the energy and the intensity of
1149 the beams to dispense the prescribed dose amount. By the point of view of the instrumen-
1150 tation and the testing on it, a more common and useful parameter is instead the rate or
1151 the fluence of particles. The conversion between the two quantity can be found thinking to
1152 the definition of dose: it is the concentration of energy deposited in tissue as a result of an
1153 exposure to ionizing radiation. Assuming total absorption of electrons in water, defined
1154 by law as the ordinary reference medium, the dose can be expressed as:

$$D[Gy] = \frac{NE[eV]}{\rho[g/cm^3]A[cm^2]x[cm]} \quad (7.1)$$

1155 After having applied the conversion of the energy from eV to J and noticed that $E/\rho x$
1156 roughly corresponds to the stopping power S of electrons in water, a simple estimation of
1157 the dose released in water is:

$$D[Gy] = 1.602 \cdot 10^{-10} N[cm^{-2}] S[MeVcm^2/g] \quad (7.2)$$

1158 **7.1 Apparatus description**

1159 The accelerator is placed in a bunker inside the hospital: to shield the outdoor from
1160 ionizing radiation the bunker has very thick walls of cementum and both the control units
1161 of the accelerator and of the detector were placed outside the bunker. For practicability
1162 reasons the power supply were the only device to be placed inside the bunker.

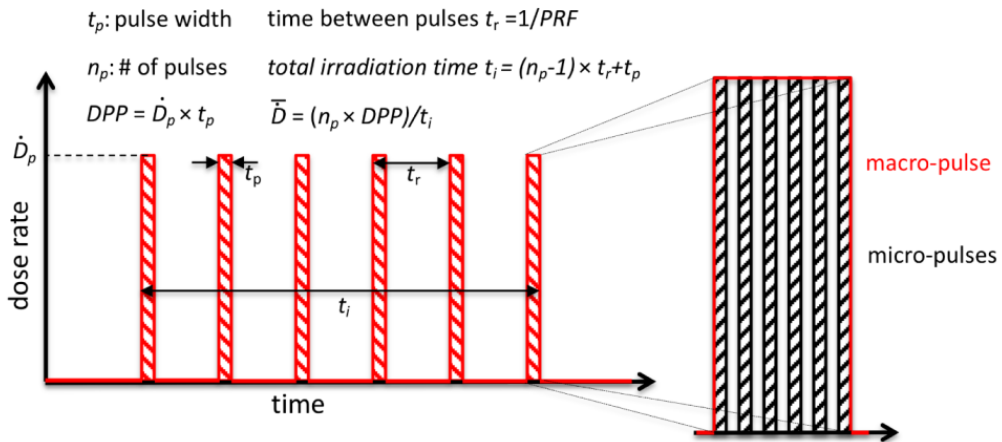


Figure 7.1: Typical beam structure of a beam with the standard characteristic quantity

\bar{D}	Dose rate (mean dose rate for a multi-pulse delivery)	0.005-10000 Gy/s
\dot{D}	Intra pulse dose rate (dose rate in a single pulse)	0.01-1 10^6 Gy/s
DDP	Dose in a single pulse	0.04-40 Gy
PRF	Pulse repetition frequency (number of pulses delivered per unit of time)	1-350 Hz
t_p	Pulse width	0.2-4 μ s
n	Number of pulses	single/pulse train

Table 7.1: The parameters that can actually be set by the control unit are the PRF, DDP, t_p and n (in particular singular irradiation or pulse train), while the other changes consequently.

7.1.1 Accelerator

The ElectronFlash accelerator is an electron Linear Accelerator (LINAC) with two energy configurations, at 7 MeV and 9 MeV, and it can reach ultra high intensity (40 Gy/pulse) keeping the possibility of accessing many different beam parameters and changing them independently from each other. This characteristic is fundamental for research in FLASH-RT, both for the medical aspects and for the studies on detectors; for example is not really clear the dependence of the efficacy of the FLASH effect on the whole dose parameters. ElectronFlash is almost the only one in the world having this characteristic, **ricontrolla sulla review, c'era qualcosa che puoi dire.** The accelerator implements a standard beam structure for RT with electrons (fig. 7.1), that is a macro pulse divided in many micropulses; the parameters used to set the dose and their range of values settable by the control unit is reported in table 7.1.

The accelerator is provided of a set of triod cannons ~ 1.2 m long and with diameters from 1 cm to 12 cm and a collimator that can be used as beam shaper to produce a squircle shape. The triode, which is made by plexiglass, must be fix to the gun during the irradiation and is needed for producing an uniform dose profile (fig.7.2) which is desired for medical purpose via the scattering of electrons with the plexiglass.

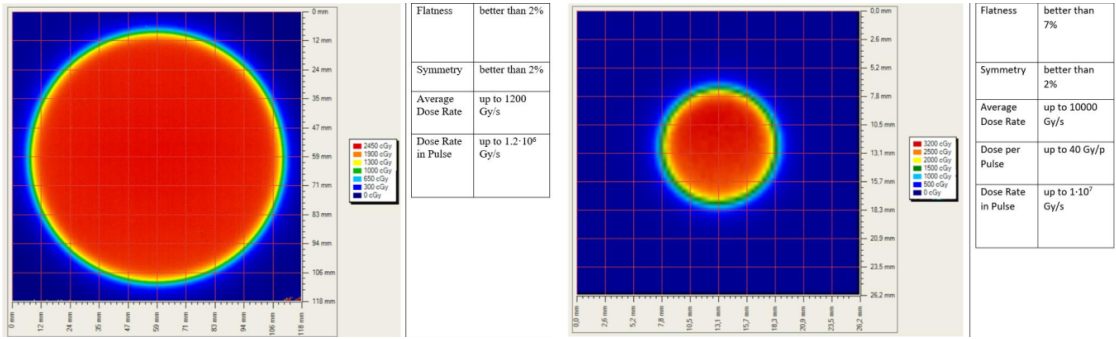


Figure 7.2: Two example of x-y isodose curves for two different triodes, 10 cm and 1 cm respectively, reported by the producer in the manual with the specific of the accelerator (S.I.T. - Sordina IORT Technologies S.p.A.). With the smaller collimator the dose rate in pulse is comparatively higher.

1180 7.1.2 Mechanical carriers

1181 The tested detector consists in one chip, the Device Under Test (DUT), mounted on a
 1182 board and connected to FPGA with same arrangement of figure 7.7. These have been
 1183 positioned vertically in front of the triode on a table specifically built for the testbeam.
 1184 The tree board have been enclosed in a box of alluminium with a window on the DUT
 1185 and with the required holes at the side to enable the biasing via cables and the connection
 1186 with the DAQ provided via ethernet cable. A trigger signal coming from the control unity
 1187 and syncronize with the pulses emitted from the beam has been also sent to the FPGA.
 1188 This signal cannot be considered a trigger signal, since being a prototypes TJ-Monopix1
 1189 has been designed to be triggerless, but the time of arrival of this signal, which is saved
 1190 by the FPGA, can allow the reconstruction of the of the arrival of the bunch during the
 1191 analysis.

1192 In order to shield the sensor from the whole particles emitted from the gun, two
 1193 alluminium collimators have been fabricated: one has been positioned at the triode exit
 1194 while the other in front of the DUT. The collimators are $t=32$ mm thick and have a
 1195 diameter d equal to 1 mm: assuming a beam divergence bigger than $d/t=1/32 = 1.8^\circ$,
 1196 which is the case, the collimator at the triode output was supposed to work as a point
 1197 source and to reduce the rate on the DUT of a factor at least $4 \cdot 10^{-4}$. The second one,
 1198 being near the DUT, was instead supposed to shield the sensor from the electrons which
 1199 have passed the first one, except for a region of 1 mm^2 configurable using *come si chiamano*
 1200 *quei cacciavitini per settare la posizione?*.

1201 7.2 Measurements

1202 Because of the dead time of TJ-Monopix1 it is not possible resolving the bunch sub-
 1203 structure and almost no one pixel can read more than a hit per bunch. I recall, indeed,
 1204 that the dead time per pixel depends on the location on the priority chain for the readout
 1205 and for each pixel $\lesssim 1 \mu\text{s}$ (fig. 7.7) are needed; therefore only a few pixels at the top of
 1206 the priority chain (at the upper left of the matrix) can fire a second time, since they in
 1207 principle can be read the first time before the end of the pulse (assuming a pulse duration
 1208 in $2 \mu\text{s}-4 \mu\text{s}$) and then can be hit again.

1209 Since resolving the single electron track is impossible, a way this sensor could be used

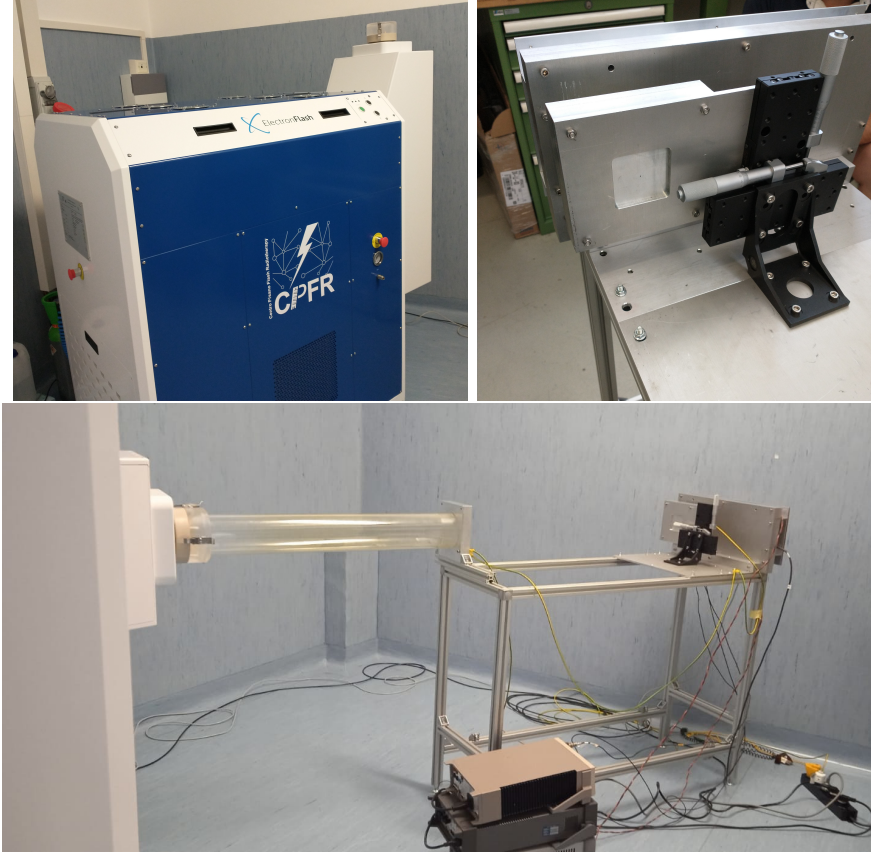


Figure 7.3: Experimental set up. (a) Electron flash accelerator: gantry rotante che consente un orientamento del fascio da 0° 90° (orizzontale / verticale) in tempo reale monitorato da un inclinometro integrato. the gun can be rotated from 90° to 0° (vertical/orizontal). (b) Collimator and DUT box. (c) Whole structure: we used the 10 cm diameter and 1.2 m long triode; the DUT which is in the box behind the two collimators is connected to the power supply units.

in such context is reducing its efficiency and taking advantage of the analog pile up and of the linearity of the analog output (ToT), in order to see a signal produced not by the single particle but by more electrons. Reducing the efficiency and the sensibility of the sensor is essential in order to decrease the high charge signal produced in the epitaxial layer: if the sensor is completely depleted the collection efficiency is closer to 1% and if the whole charges produced by a MIP, $80 \text{ e}^-/\mu\text{m}$ about, are collected, the saturation limit is soon reach. Then a condition where there is a partial recombination of the center electron-hole created in the bulk is desiderable. On the other hand, the smaller the output signal value and the higher the rate the detector can cope with: indeed, the rollover constitutes a limit for the usage of the analog output. With the standard configuration of the FE parameters and the epitaxial layer completely depleted, a MIP produces a ToT out of range of representation of 6-bit; so as to obtain smaller output signals one can operate on the reduction of the gain of the preamplifier or on the pulse velocity of returnig to the baseline. Recalling the results in section 6.1.4, I have shown that concerning the PMOS flavor 1, reducing the bias from -6 V to 0 V brings a reduction of efficiency down to 40 %, and a reduction in the gain of a factor $\sim 1/3$, while the reduction of the gain of the preamplifier allows a reduction of **circa 10, ma da controllare**.

1227 In order to taking advantage of the analog pile up and integrating the charge, for
 1228 semplicity assume of two electrons, the second one must hit the pixel before the ToT goes
 1229 under the threshold. The general condition is then $\overline{\Delta T} < \overline{ToT}$, but if a high $P_\mu(n \geq 1)$ is
 1230 required, a lower $\overline{\Delta T}$ may be desired:

$$P(n \geq 1) = \sum_{n=1}^{\infty} \frac{e^{-\mu} \mu^n}{n!} = 1 - P(0) = 1 - e^{-\mu} \quad (7.3)$$

1231

$$\mu = \frac{\overline{ToT}}{\overline{\Delta T}} \quad (7.4)$$

1232 If a $P_\mu(n \geq 1) = 99\%$ then the $\overline{\Delta T}$ must be $\sim 0.22 \overline{ToT}$. The ToT is in range [0,64] but
 1233 since the rollover must be avoided, the \overline{ToT} must be lower than 32, and then the minimum
 1234 rate on the pixel must be 1.25 MHz.

1235 During the testbeam many runs have been performed, spanning the energy, the dose
 1236 per pulse and the four possible configurations with/without the collimators. We have used
 1237 the PMOS flavor 1 in the standard configuration: we have biased the PWELL and PSUB
 1238 at -6 V and set the standard default FE parameters reported in table ???. During all the
 1239 acquisitions we have used pulses with t_p of 4 μm and with the smallest PRF settable, which
 1240 is 1 Hz, in order to start in the most conservative working point exluding the digital pile
 1241 up of events from different bunch: even if the whole matrix turns on and there are 25000
 1242 hits, the total readout time corresponding to 25 ms is still lower than the time between two
 1243 consecutive pulses. The readout starts with the trailing edge of the first pulse going down
 1244 the threshold, ~ 50 clk = 1.25 μs after this moment the FREEZE signal is sent to the whole
 1245 matrix, and the trasmittion of the data to the EoC begins. The hits read are the ones
 1246 whose TE occurred during the 50 clk counts; the ones, instead, whose TE occur during the
 1247 FREEZE are stored in the pixel memory and read during a second readout. Obviously
 1248 since the readout of the fist sub-pulse finishes much later than the bunch ends up, each
 1249 pixel can be store only one hit. An example of the two sub-pulses is shown in figure ???:
 1250 in the acquisition we injected 5 pulses with both the collimators mounted on the table.
 1251 Looking at the spectrum **si vede che lo spettro del secondo pulse ha una coda più lunga a**
 1252 **destra: questo è dovuto al fatto che le hit con tot lungo hanno il TE che cade durante il**
 1253 **FREEZE e quindi vengono lette durante il secondo impulso.** On the other hand the 2D
 1254 histograms, being uniform and not showing disomogenities, suggest that the collimators
 1255 do not shield all the particles: this was due to a photon background higher than expected.
 1256 When we have put aside the collimators, instead, the fluence was too high that **the whole**
 1257 **matrix turns on in 50 clk counts; then the 2 pulses substructure no more appears (fig. 7.6).**
 1258 **CONTROLLA PERCHÈ PORTEBBE ESSERE UNA CAZZATA**

1260 After the testbeam a simulation of the emission of electrons from the accelerator and
 1261 their path across the triode and the collimators has been developed via Geant-4 **come si**
 1262 **ringrazia il lavoro di qualcuno in maniera formale?** The high background we saw although
 1263 the collimators were mainly produced by electrons Bremsstrahlung during the transition
 1264 through the alluminium collimators. **dalla simulazione si è visto che nessun elettrone**
 1265 **arriva sul chip quando ci sono montati i collimatori, mentre nel caso senza collimatori gli**
 1266 **eventi sono sostanzialmente tutti elettronni (frazione di fotoni prodotti in aria è?).** The
 1267 photons' simulated spectrum in the three configurations are shown in figure ???. **confronto**
 1268 **con quello che vedo nello spettro sopra: dati.**

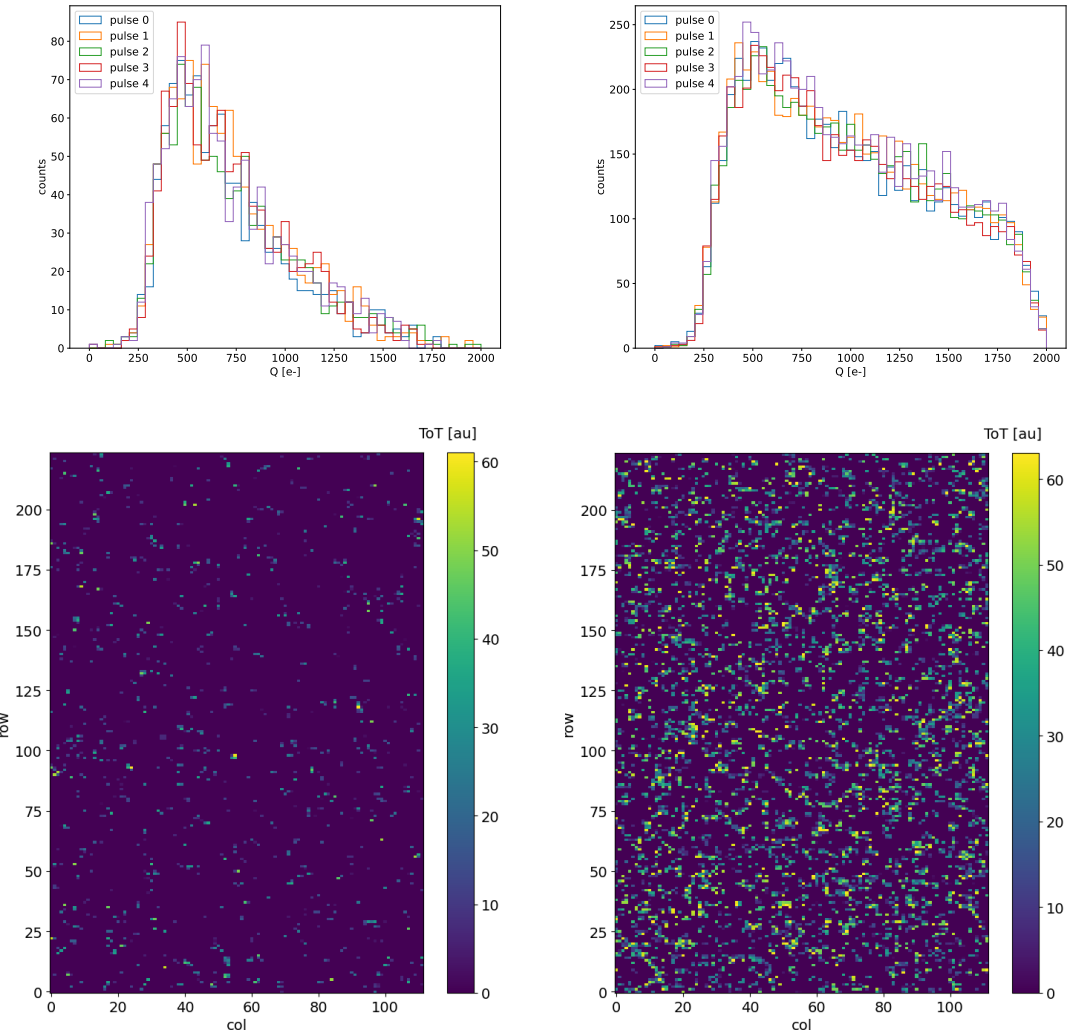


Figure 7.4: Acquisition with both the collimators: 5 pulses at $DDP=0.07$ Gy. (a) Spectrum of the charge released in the sensor: to apply the conversion I used the information found in the previous chapter. (b) 2D histogram of the ToT of the hits arrived in the sub-pulses.

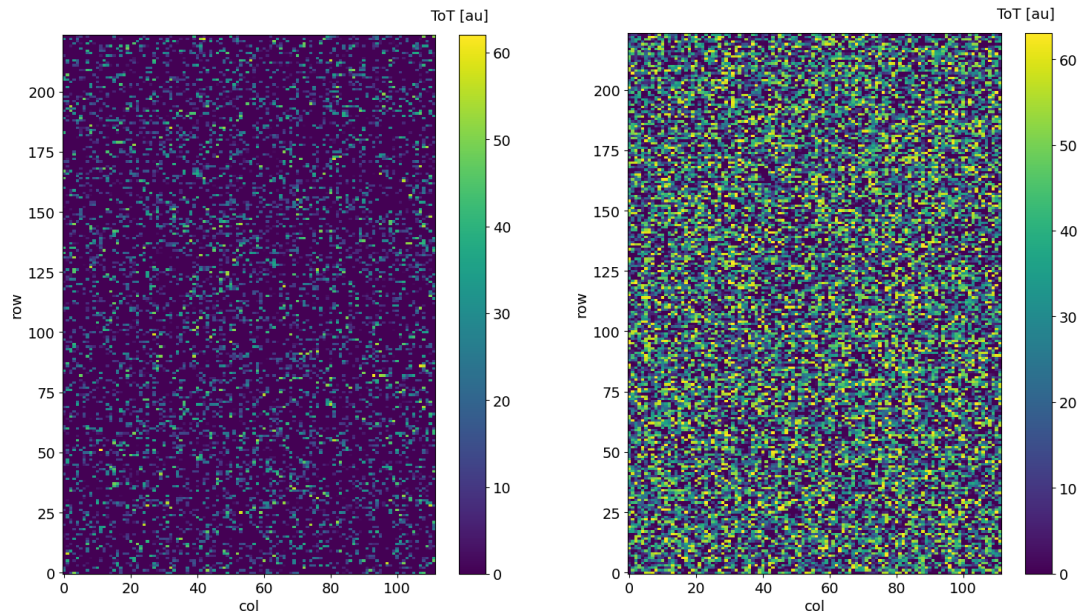


Figure 7.5: Acquisition with both the collimators: 5 pulses at DDP=0.6 Gy. 2D histogram of the ToT of the hits arrived in the sub-pulses. Compared with the previous maps, since the DDP is much higher, more pixels turn on.

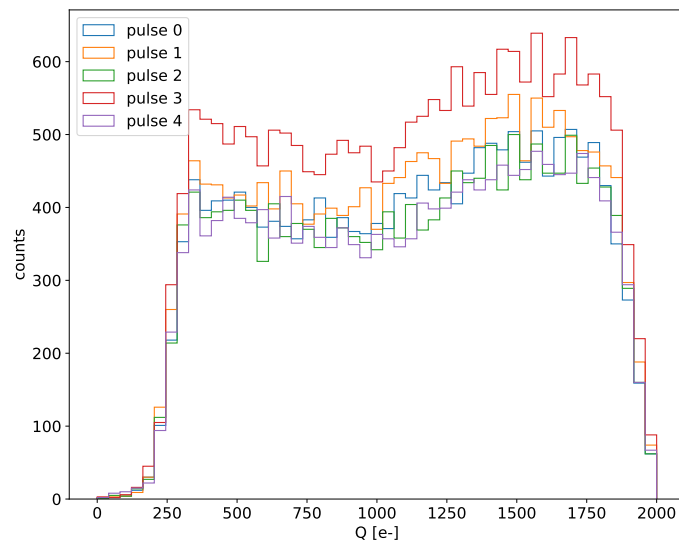


Figure 7.6: Acquisition without any collimator: 5 pulses at DDP=0.04 Gy.

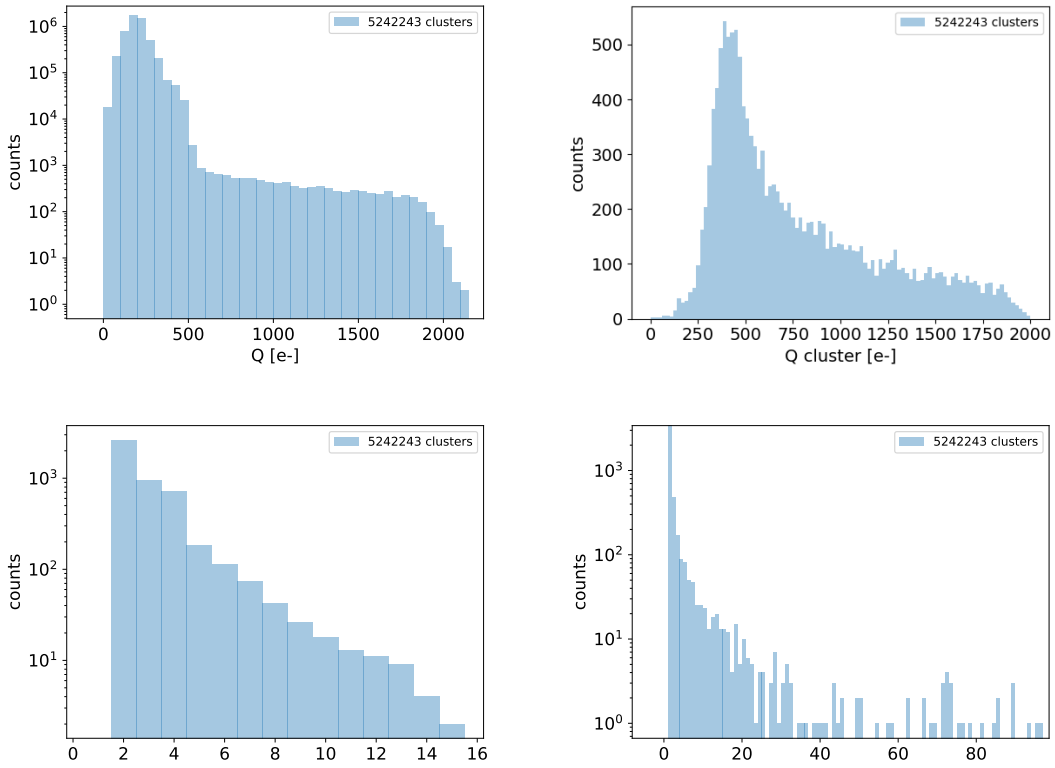


Figure 7.7: plot dei raggi cosmici da rigenerare

- 1269 • plot n di eventi che vedo con le diverse configurazioni
- 1270 • simulazione surya
- 1271 • confronta con misure dello spettro che vediamo senza e con collimatori.

1272 7.2.1 MIP spectrum using cosmic rays as source

1273 Since a MIP should produce about 2 ke- in the epitaxial layer, it should provide a signal
 1274 that in our conditions (full depletion and high gain) rolls over: in this situation making
 1275 prediction on the spectrum expected for MIPs becomes hard. Therefore, in order to
 1276 compare the spectrum observed at the testbeam with one certainly produced by MIP I
 1277 have made some acquisitions without any radioactive source, in order to look at the cosmic
 1278 ray events. To be confident with having selected MIPs from cosmic rays and cut the noise, I
 1279 have selected only the events with multiple hits: these events are mainly clusters produced
 1280 by the same impinging particle since the random coincidence probability is very low. In
 1281 fact the cosmic rays and noise rates on the whole matrix are respectively 0.02 Hz and
 1282 $\sim\text{Hz}$, the dead time in such a low occupancy condition can be always approximated with
 1283 $1\text{ }\mu\text{m}$ (this is not completely true for multiple hits events for which the priority chain
 1284 should be considered), the random coincidence rate is 10^{-8} Hz . Come mai lo spettro in
 1285 lab è diverso da quello visto con gli elettroni da 9 MeV al santa chiara? Chiedi a Surya il
 1286 rate visto sul detector senza collimatori.

₁₂₈₇ **Appendix A**

₁₂₈₈ **Pixels detector: a brief overview**

₁₂₈₉ **A.1 Radiation damages**

₁₂₉₀ Radiation hardness is a fundamental requirement for pixels detector especially in HEP
₁₂₉₁ since they are almost always installed near the interaction point where there is a high
₁₂₉₂ energy level of radiation. At LHC the ϕ_{eq} per year in the innermost pixel detector is
₁₂₉₃ $10^{14} n_{eq}/cm^2$; this number reduces by an order passing to the outer tracker layer [2] pag
₁₂₉₄ 341 Wermes. Here the high fluence of particles can cause a damage both in the substrate
₁₂₉₅ of the detector and in the superficial electronics.

₁₂₉₆ The first one has a principal non ionizing nature, due to a non ionizing energy loss
₁₂₉₇ (NIEL), but it is related with the dislocation of the lattice caused by the collision with
₁₂₉₈ nuclei; by this fact the NIEL hypothesis states that the substrate damage is normalized to
₁₂₉₉ the damage caused by 1 MeV neutrons. Differently, surface damages are principally due
₁₃₀₀ to ionizing energy loss.

₁₃₀₁ **DUE PAROLE IN PIÙ SUL SURFACE DAMAGE** A charge accumulation in oxide
₁₃₀₂ (SiO_2) can cause the generation of parasitic current with an obvious increase of the 1/f
₁₃₀₃ noise. Surface damages are mostly less relevant than the previous one, since with the de-
₁₃₀₄velopment of microelectronics and with the miniaturization of components (in electronic
₁₃₀₅ industry 6-7 nm transistors are already used, while for MAPS the dimensions of compo-
₁₃₀₆nents is around 180 nm) the quantity of oxide in circuit is reduced.

₁₃₀₇ Let's spend instead two more other words on the more-relevant substrate damages:
₁₃₀₈ the general result of high radiation level is the creation of new energy levels within the
₁₃₀₉ silicon band gap and depending on their energy-location their effect can be different, as
₁₃₁₀ described in the Shockley-Read-Hall (SRH) statistical model. The three main consequence
₁₃₁₁ of radiation damages are the changing of the effect doping concentration, the leakage
₁₃₁₂ current and the increasing of trapping probability.

₁₃₁₃ **Changing of the effective doping concentration:** is associated with the cre-
₁₃₁₄ation/removal of donors and acceptors center which trap respectively electrons/holes from
₁₃₁₅ the conduction band and cause a change in effective space charge density. Even an in-
₁₃₁₆version (p-type becomes n-type¹) can happen: indeed it is quite common at not too high
₁₃₁₇ fluences ($\phi_{eq} 10^{12-13} n_{eq} cm^{-2}$). A changing in the doping concentration requires an adjust-
₁₃₁₈ment of the biasing of the sensor during its lifetime (eq.2.1) and sometimes can be difficult
₁₃₁₉keeping to fully deplete the bulk.

₁₃₂₀ **Leakage current:** is associated with the generation-recombination centers. It has

¹L'INVERSIONE OPPOSTA NON CE L'HAI PERCHÈ?

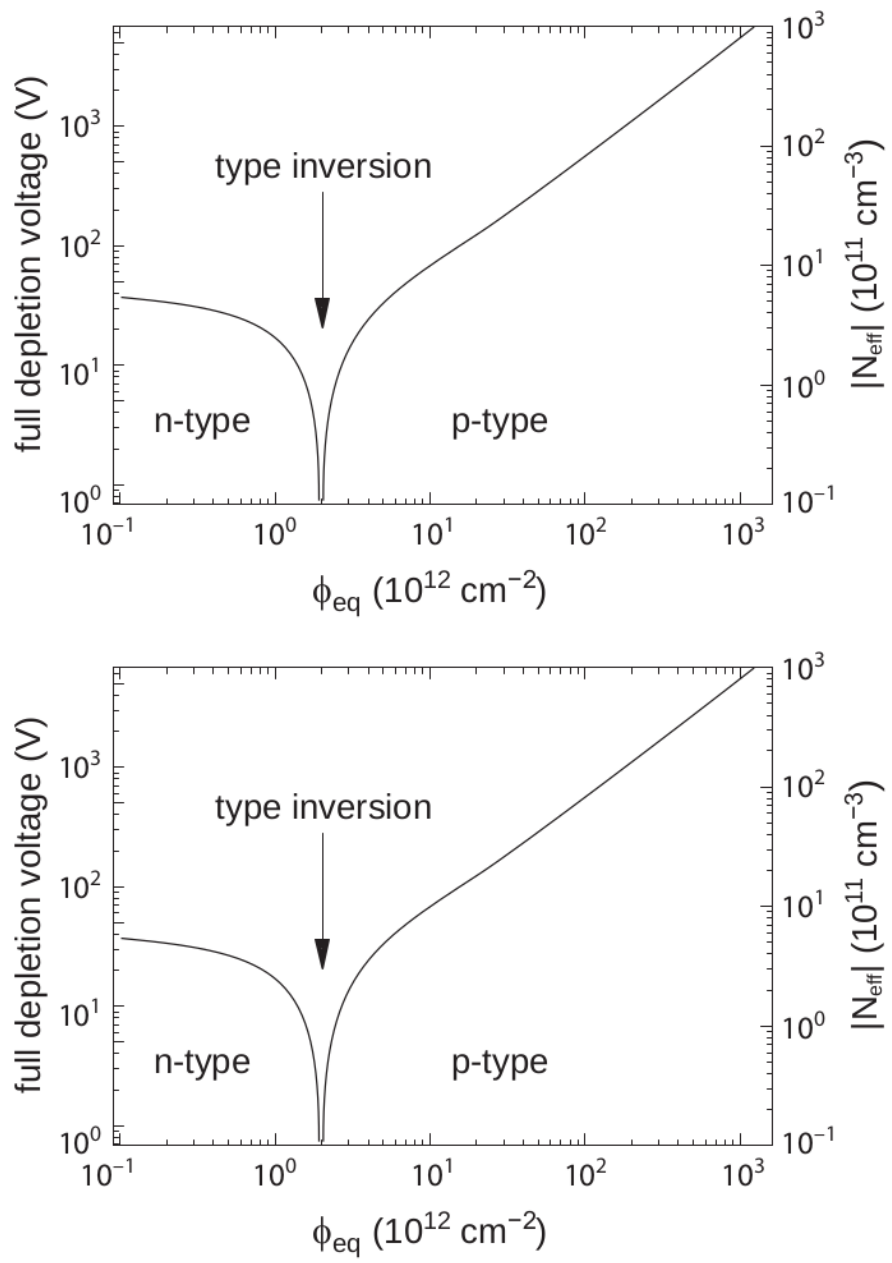


Figure A.1: 1b

1321 a strong dependence with the temperature ($I_{leak} \propto T^2$), whose solution is therefore to
1322 operate at lower temperature.

1323 **Increase of trapping probability:** since the trapping probability is constant in the
1324 depleted region, the collected charge decreases exponentially with the drift path. The
1325 exponential coefficient, that is the mean trapping path, decreases after irradiation and
1326 typical values are 125-250 μm and must be compared with the thickness of the depleted
1327 region which () corresponds to the mean drift path.

1328 Different choices for substrate resistivity, for junctions type and for detector design are
1329 typically made to fight radiation issues. Some material with high oxygen concentration
1330 (as crystal produced using Czochralki (Cz) or float-zone (Fz) process (**CONTROLLA**
1331 **LA DIFFERENZA TRA I DUE**)) for example, show a compensation effect for radiation
1332 damage; another example is the usage of n+ -in-p/n sensors (even if p+ -in-n sensors are
1333 easier and cheaper to obtain) to get advantage of inversion/to have not the inversion (since
1334 they are already p-type). After inversion the n+p boundary, coming from n+ in-n, but to
1335 keep using the sensor the depletion zone still must be placed near the diode.

1336 Single Event Upset, in sostanza è quando un bit ti cambia valore (da 0 a 1 o viceversa)
1337 perché una particella deposita carica nell'elettronica che fa da memoria registro/RAM/....
1338 Questo tipo di elettronica ha bisogno di un sacco di carica prima che il bit si "fippi"
1339 (cambi valore), infatti tipicamente per avere un SEU non basta una MIP che attraversa
1340 esattamente quel pezzo di chip in cui è implementata la memoria, ma un adrone che faccia
1341 interazione nucleare producendo più carica di quanto farebbe una MIP. Questo metodo pur
1342 essendo più comodo richiede less amount of area ha però come drawback che il registro può
1343 essere soggetto a SEU problema non trascurabile in acceleratori come HL-LHC adronici

¹³⁴⁴ Bibliography

- 1345 [1] W. Snoeys et al. “A process modification for CMOS monolithic active pixel sensors
1346 for enhanced depletion, timing performance and radiation tolerance”. In: (2017).
1347 DOI: <https://doi.org/10.1016/j.nima.2017.07.046>.
- 1348 [2] H. Kolanoski and N. Wermes. *Particle Detectors: Fundamentals and Applications*.
1349 OXFORD University Press, 2020. ISBN: 9780198520115.
- 1350 [3] E. Mandelli. “Digital Column Readout Architecture for 10.1109/NSSMIC.2009.5402399
1351 the ATLAS Pixel 0.25 um Front End IC”. In: (2002).
- 1352 [4] M. Garcia-Sciveres and N. Wermes. “A review of advances in pixel detectors for
1353 experiments with high rate and radiation”. In: (2018). DOI: <https://doi.org/10.1088/1361-6633/aab064>.
- 1355 [5] C. Marinas. “The Belle-II DEPFET pixel detector: A step forward in vertexing in the
1356 superKEKB flavour factory”. In: (2011). DOI: [doi:10.1016/j.nima.2010.12.116](https://doi.org/10.1016/j.nima.2010.12.116).
- 1357 [6] J. Baudot. “First Test Results Of MIMOSA-26, A Fast CMOS Sensor With Inte-
1358 grated Zero Suppression And Digitized Output”. In: (2010). DOI: [doi:10.1109/NSSMIC.2009.5402399](https://doi.org/10.1109/NSSMIC.2009.5402399).
- 1360 [7] A. Dorokhov. “High resistivity CMOS pixel sensors and their application to the
1361 STAR PXL detector”. In: (2011). DOI: [doi:10.1016/j.nima.2010.12.112](https://doi.org/10.1016/j.nima.2010.12.112).
- 1362 [8] Giacomo Contin. “The STAR MAPS-based PiXeL detector”. In: (2018). DOI: <https://doi.org/10.1016/j.nima.2018.03.003>.
- 1364 [9] Nolan Esplen. “Physics and biology of ultrahigh dose-rate (FLASH) radiotherapy:
1365 a topical review”. In: (2020). DOI: <https://doi.org/10.1088/1361-6560/abaa28>.
- 1366 [10] M. Dyndal et al. “Mini-MALTA: Radiation hard pixel designs for small-electrode
1367 monolithic CMOS sensors for the High Luminosity LHC”. In: (2019). DOI: <https://doi.org/10.1088/1748-0221/15/02/p02005>.
- 1369 [11] M. Barbero. “Radiation hard DMAPS pixel sensors in 150 nm CMOS technology
1370 for operation at LHC”. In: (2020). DOI: <https://doi.org/10.1088/1748-0221/15/05/p05013>.
- 1372 [12] K. Moustakas et al. “CMOS Monolithic Pixel Sensors based on the Column-Drain
1373 Architecture for the HL-LHC Upgrade”. In: (2018). DOI: <https://doi.org/10.1016/j.nima.2018.09.100>.
- 1375 [13] I. Caicedo et al. “The Monopix chips: depleted monolithic active pixel sensors with
1376 a column-drain read-out architecture for the ATLAS Inner Tracker upgrade”. In:
1377 (2019). DOI: <https://doi.org/10.1088/1748-0221/14/06/C06006>.

- 1378 [14] D. Kim et al. “Front end optimization for the monolithic active pixel sensor of the
1379 ALICE Inner Tracking System upgrade”. In: *JINST* (2016). DOI: doi:10.1088/
1380 1748-0221/11/02/C02042.
- 1381 [15] L. Pancheri et al. “A 110 nm CMOS process for fully-depleted pixel sensors”. In:
1382 (2019). DOI: <https://doi.org/10.1088/1748-0221/14/06/c06016>.
- 1383 [16] L. Pancheri et al. “Fully Depleted MAPS in 110-nm CMOS Process With 100–300-
1384 um Active Substrate”. In: (2020). DOI: 10.1109/TED.2020.2985639.